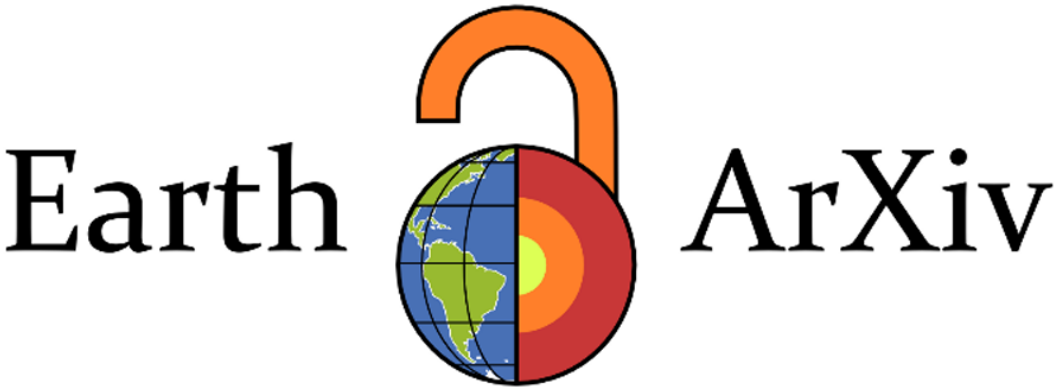

Beyond calcite: Crude-urease enzyme-induced carbonate precipitation reveals metal-specific crystallogenetic pathways

Dickinson, Heloísa [a,b]; MacDonald, John[a]; Pérez, Carlos Alberto [c]; Toney, Jaime L.[a]
[a]School of Geographical and Earth Sciences, University of Glasgow
[b]School of Social and Environmental Sustainability, University of Glasgow
[c]Brazilian Synchrotron Light Laboratory (LNLS), Brazilian Centre for Research in Energy and Materials (CNPEM)

*Corresponding author. E-mail: heloisa.dickinson@glasgow.ac.uk

---

Abstract

During carbonate biomineralization, metal identity governs phase selection and metal partitioning, directing contaminants into fundamentally different crystallogenetic pathways even where bulk removal efficiencies remain high. However, the mechanisms controlling this divergence remain incompletely understood. Here, we compare the mineralogical fate of Pb, Co and Cr under standardized urease-driven enzyme-induced carbonate precipitation (EICP) using a crude soybean-derived urease extract across a metal concentration range of 2–20 mM. Metal retention pathways were investigated using SEM–EDS, powder X-ray diffraction with Rietveld refinement, and synchrotron Nano-XRF mapping. Despite identical precipitation conditions, the three metals followed markedly different mineralogical trajectories. Pb and Co systems maintained high alkalinity (final pH ≈ 8.1–8.2) and high removal efficiencies (>99% for Pb and 97–98% for Co), yet their mineralogical evolution differed fundamentally. Pb exhibited a concentration-dependent evolution characterized by the progressive stabilization of discrete cerussite populations within otherwise calcite-dominated assemblages. Cerussite was absent at 2 mM, accounted for ~3 wt% at intermediate loadings, and reached ~6 wt% at 20 mM, coexisting with $CaCO_3$ domains exhibiting progressive chemical zonation and variable Pb incorporation. In contrast, Co remained diffusely associated with calcite-dominated precipitates across all concentrations, showing no evidence of chemical zonation or discrete cobalt carbonate phases. Cr exhibited consistently lower final pH (7.5–7.8) and the greatest departure from carbonate-controlled mineralization. Progressive inhibition of ureolysis with increasing Cr loading reduced carbonate precipitation and lowered removal efficiency from 97% at T1 to 87% at T3. At the highest loading, Cr-rich, Ca-poor domains developed alongside elongated prismatic crystals and Ca–S-rich precipitates with gypsum-like morphologies, collectively indicating a shift away from carbonate-dominated precipitation pathways. Together, these findings establish metal identity as a first-order control on carbonate biomineralization, governing phase selection and metal partitioning independently of bulk removal efficiency. Despite these divergent mineralogical outcomes, sunflower-like radial aggregates recurred across all systems, except Cr-T3, suggesting a shared, plausibly precursor-mediated crystallization framework. Removal efficiency is therefore a poor proxy for mineralogical fate, with important implications for predicting contaminant mobility and the long-term stability of biomineralization-based immobilization strategies.

Keywords
Carbonate biomineralization; Crystal chemistry; Phase selection; Metal partitioning; Enzyme-induced carbonate precipitation

1. Introduction

Carbonate biomineralisation is one of the most widespread mineral-forming processes in natural systems, shaping the formation of sediments, soils and freshwater carbonates while regulating the cycling of carbon and metals across Earth's surface (Lowenstam & Weiner, 1989; Weiner & Dove, 2003; Weiner & Addadi, 2011). The ability to reproduce these processes under ambient conditions has led to the development of enzyme-induced carbonate precipitation (EICP), where urease-catalysed urea hydrolysis generates carbonate supersaturation and promotes rapid $CaCO_3$ precipitation. EICP operational simplicity and broad applicability have attracted considerable attention for applications including soil improvement, biocementation, contaminant immobilisation and carbon sequestration (Yasuhara et al., 2012; Hamdan & Kavazanjian, 2016; Moghal et al., 2020; Bian et al., 2024).

Most studies evaluating metal immobilisation by EICP focus on removal efficiency, whereas the fate of the retained metals receives considerably less attention. Consequently, metal retention is commonly discussed in terms of cation substitution, adsorption or surface complexation, yet the individual contribution of these mechanisms is rarely investigated or resolved through detailed mineralogical characterization. As a result, the mineralogical controls governing metal partitioning during carbonate precipitation remain largely unresolved (Bian et al., 2024; Zeng et al., 2025). In particular, it remains unclear whether different metals follow comparable mineralisation pathways under otherwise identical carbonate-forming conditions, limiting our ability to predict their mineralogical fate and long-term stability.

Decades of research on carbonate mineralogy have shown that individual metals interact differently with growing carbonates, influencing nucleation, crystal growth, phase selection and crystal chemistry according to their crystal-chemical properties (McBride, 1980; Stipp et al., 1992; Reeder, 1996). Experimental and crystallographic studies during the 1980s and 1990s established many of these fundamental controls (Paquette & Reeder, 1990, 1995; Paquette et al., 1993), yet they have rarely been incorporated into mechanistic interpretations of EICP.

Pb, Co and Cr provide an effective framework for examining these controls because they represent contrasting crystal-chemical behaviours in carbonate systems. Pb^{2+} shows strong affinity for carbonate surfaces but limited compatibility with the calcite lattice, frequently leading to the formation of discrete Pb-carbonate phases such as cerussite (Reeder, 1996; Sturchio et al., 1997). Co^{2+} more closely resembles Ca^{2+} in charge and ionic radius, although its incorporation into calcite remains energetically restricted and preferentially occurs at defects and growth steps (Lorens, 1981; Paquette & Reeder, 1995). Cr(III), by contrast, is largely incompatible with calcite and is commonly retained through non-substitutional mechanisms, including adsorption and hydroxide-

or oxide-associated phases, while simultaneously perturbing carbonate crystallisation (García-Sánchez & Álvarez-Ayuso, 2002; Fang et al., 2022). Although these contrasting behaviours are well recognised in carbonate mineralogy, they have not been systematically investigated under identical EICP conditions.

Here, we compare the crystallogenetic evolution of Pb, Co and Cr during urease-driven carbonate biomineralisation using a crude soybean-derived enzyme extract. Combining scanning electron microscopy with energy-dispersive spectroscopy (SEM–EDS), powder X-ray diffraction coupled with Rietveld refinement, and synchrotron Nano-XRF mapping, we identify the mineral phases formed and investigate the pathways by which each metal partitions during carbonate precipitation. The results reveal systematic differences in phase selection and metal partitioning that reflect the crystal-chemical behaviour of each element. These observations provide a mineralogical framework for understanding metal immobilisation during EICP and improve the mechanistic basis for predicting long-term sequestration behaviour.

1.1. Crystallogenetic controls on phase selection and metal partitioning during EICP

Enzyme-induced carbonate precipitation (EICP) is driven by urease-catalysed urea hydrolysis, which elevates pH and generates dissolved inorganic carbon, thereby increasing carbonate alkalinity and promoting $CaCO_3$ supersaturation under ambient conditions in the presence of Ca^{2+} (Nemati & Voordouw, 2003; Whiffin et al., 2007; Kidanemariam et al., 2024). While urease is the primary driver of alkalinity generation, crude enzyme extracts also introduce organic macromolecules that can modify nucleation environments, growth dynamics, and mineral–solution interactions.

Carbonate precipitation under EICP conditions can proceed through multiple crystallogenetic pathways with contrasting capacities for metal uptake. These include substitutional incorporation within the calcite lattice (McBride, 1980; Reeder, 1996), defect- and step-assisted coprecipitation during crystal growth (Stipp et al., 1992; Paquette & Reeder, 1995), and adsorption at crystal surfaces governed by aqueous speciation and surface complexation reactions (Stumm & Morgan, 1996; Callagon et al., 2017). Where crystal-chemical compatibility is limited or metal carbonate solubility is low, metals may segregate into discrete carbonate phases or be diverted into non-carbonate secondary minerals such as hydroxides, phosphates, or mixed hydroxy-carbonates (Langmuir, 1997; Bourg & Sposito, 2007).

Three first-order controls constrain metal behaviour during carbonate biomineralization. The first is crystal-chemical compatibility, which governs the energetic feasibility of substitution at Ca^{2+} sites and the extent to which metals can be accommodated within carbonate lattices (Reeder, 1996; Paquette & Reeder, 1995). The second is metal-specific aqueous speciation and hydrolysis behaviour, which influences carbonate availability, competitive precipitation pathways, and sensitivity to redox and pH conditions (Stumm & Morgan, 1996; Langmuir, 1997). The third is interaction with early mineral precursors and active growth surfaces: transient amorphous or poorly ordered phases, often stabilised by organic components, can exert strong kinetic control

on metal partitioning and persistence within the final mineral assemblage (Lowenstam & Weiner, 1989; Addadi & Weiner, 1992; Beniash et al., 1997).

Within this framework, metal partitioning during EICP is inherently element-specific and pathway-dependent. Identical bulk reaction conditions may therefore yield similar removal efficiencies while producing fundamentally different mineralogical outcomes, and similar bulk removal efficiencies cannot be assumed to reflect equivalent crystallogenetic trajectories or long-term sequestration stability. Identifying the mineral phases responsible for metal sequestration is therefore fundamental to understanding not only how metals are retained, but also how efficiently and how persistently they remain immobilised under changing environmental conditions.

2. Materials and Methods

Full experimental details, instrumental settings, and data-analysis procedures are provided in the Supplementary Material; essential methodological information is summarised below. Laboratory analyses were conducted at the University of Glasgow, with the exception of synchrotron-based measurements, which were performed at the Brazilian Synchrotron Light Laboratory (LNLS), part of the Brazilian Center for Research in Energy and Materials (CNPEM), Campinas, Brazil and the ammonium concentrations that were assessed in the Laboratory of Geochemistry of the University of Edinburgh.

2.1. Materials and reagents

Urea (NH_2CONH_2 ≥ 99.0%), calcium chloride dihydrate ($CaCl_2 \cdot 2H_2O$ ≥ 99.0%), and all metal salts used to prepare stock solutions ($PbCl_2$ 99.999%, $CoCl_2$ ≥ 98.0%, $Cr_2(SO_4)_3 \cdot xH_2O$ ≥ 98.0%) were of analytical grade and used as received; deionised water (18.2 MΩ·cm) was used in all experiments.

2.2. Preparation of crude urease extract

The crude urease extract was prepared using an aqueous soybean extraction procedure. 80 grams of whole soybeans were soaked in deionised water, blended to a final volume of 1 L, and allowed to stand overnight at room temperature. The mixture was processed using a masticating juicer (Fridja f1900) to separate liquid and solid fractions. Calcium chloride was then added to the liquid fraction to a final concentration of approximately 0.06 M to promote protein precipitation. After settling for 2h at room temperature, the supernatant was decanted, centrifuged (3700 rpm, 5 min, 4 °C), and filtered using Grade 2 filter paper. Urease activity was quantified using the urea hydrolysis assay described by Whiffin (2004) and averaged 3.2 ± 0.5 mM urea min^{-1}. The crude extract was used immediately following activity measurements to minimise potential loss of enzymatic activity.

2.3. Carbonate biomineralization experiments

Carbonate biomineralization experiments were conducted by mixing equal volumes (83.4 mL each) of crude urease extract (CUE), an aqueous solution containing $CaCl_2$ (1 M) and Pb, Co, or Cr at target concentrations of 2 mM (T1), 5 mM (T2), or 20 mM (T3), and a 1 M urea solution. Each treatment was performed in quintuplicate. The resulting reaction mixtures were aliquoted into 50 mL polypropylene centrifuge tubes and incubated at 25 °C for 72 h under static conditions.

Following incubation, suspensions were left to cure at room temperature for an additional 7 days. After curing, solid phases were recovered by paper filtration, rinsed with ultrapure water, and dried in an oven at 37°C for 24 h prior to mineralogical characterisation.

2.4. Aqueous chemistry

Initial dissolved metal concentrations (C_0) were taken as the nominal concentrations of the prepared stock solutions and were verified by analysing untreated control solutions. Following curing and solid–liquid separation, supernatant samples were collected to determine residual dissolved metal concentrations (C_f), pH and ammonium concentrations.

pH was measured in triplicate in both the initial reaction mixture and the final supernatant following curing using a Mettler-Toledo FiveEasy F20 probe.

Ammonium concentrations were determined using the salicylate colorimetric method on a SEAL AutoAnalyzer AA3 and were measured once per experiment for a representative sample to confirm urease activity and urea hydrolysis during the precipitation process, serving as a qualitative process indicator rather than a quantitative variable.

For dissolved metal analysis, aliquots were acidified to 2% (v/v) HNO_3 and analysed in triplicate by inductively coupled plasma optical emission spectrometry (ICP-OES; Agilent 5900 ICP-OES).

2.5. SEM–EDS analysis

Scanning electron microscopy (SEM) analyses were conducted on the precipitates to characterise morphology and elemental distribution. For morphological imaging, samples were gently dispersed onto carbon adhesive tabs mounted on aluminium stubs and sputter-coated with a thin Au/Pd layer to minimise charging and enhance secondary-electron contrast.

For chemical analyses, including semi-quantitative energy-dispersive X-ray spectroscopy (EDS) and elemental mapping, separate aliquots of the powdered precipitates were mounted on carbon tabs and coated with conductive carbon to avoid spectral interference from metallic coatings.

EDS data were interpreted semi-quantitatively. Owing to matrix effects, particle orientation and the multiphase nature of the precipitates, absolute quantification was

not attempted. Instead, EDS measurements and elemental maps were used to assess relative metal enrichment, identify discrete metal-bearing phases, and characterise compositional heterogeneity.

2.6. Powder X-ray diffraction and Rietveld refinement

Powder X-ray diffraction data were acquired using a Malvern Panalytical Empyrean multipurpose diffractometer equipped with a Cu sealed-tube X-ray source, multicore iCore/dCore motorised optics, a hybrid monochromator, a focusing mirror, and a PIXcel3D detector, operated in reflection geometry at room temperature. Phase identification and quantitative analysis were performed by Rietveld refinement using Profex BGMN (Doebelin & Kleeberg, 2015). To evaluate potential lattice incorporation of Cr, Pb and Co, custom calcite structural models (CIFs) representing theoretical metal substitutions of ≤5, 5–10 and 10–15% were generated specifically for this study and included in the refinement. These models were used as refinement constructs to assess whether the experimental diffraction data were more consistent with progressively distorted calcite structures or with discrete secondary mineral phases, rather than to quantify true bulk solid-solution compositions.

2.7. Synchrotron nano-XRF mapping

Synchrotron-based nano-XRF elemental mapping analyses of Ca, Co, and Pb were conducted at CARNAÚBA (Coherent X-Ray Nanoprobe BeAmline) X-ray nanoprobe beamline (Tolentino et al., 2023) of the Brazilian Synchrotron Light Laboratory (Sirius-LNLS, Brazil) to characterise elemental distributions of the precipitates. The experiment used the TARUMÃ endstation (Tolentino et al., 2019) of the beamline where a small x-ray beam of ~ 300 nm in size could be achieved using a pair of elliptical mirrors in a Kirkpatrick-Baez (KB) configuration. XRF maps of Ca and Co were recorded using a monochromatic beam of E=7769 eV, just above the energy of the Co K-absorption edge ($E_{abs\text{-}K}$=7708 eV), whereas for Pb, measurements were performed at E=13100 eV, just above the Pb L_3 absorption edge ($E_{abs\text{-}L3}$ = 13035 eV). All XRF images were processed using the PyMCA software (Solé et al., 2007), a special program for X-ray fluorescence analysis developed by the ESRF synchrotron facility in Grenoble, France.

3. Results

3.1. System-level geochemical response during EICP

System-level geochemical parameters (pH, ammonium production, precipitate mass, and metal removal efficiency) were first evaluated to establish the evolution of EICP conditions across treatments, before metal-specific analysis of immobilisation behaviour and mineralogical pathways.

In Pb^{2+}-amended systems, final pH values remained consistently high (≈8.2) across all metal loadings (T1–T3) and closely matched those of the metal-free control (Fig. 1a). Ammonium concentrations were similarly elevated, typically between ~3,500 and 3,700 ppm (Fig. 1b). Precipitate masses in Pb^{2+} treatments were comparable to the control and varied only slightly with increasing metal concentration (~1.80–1.84 g; Fig. 1c). Correspondingly, Pb removal efficiencies remained consistently high (>99%) across all treatments (Fig. 1d).

In Co^{2+}-amended systems, final pH values also remained elevated (≈8.1) across all loadings, comparable to Pb^{2+} treatments and the control (Fig. 1a). Ammonium production was similarly sustained, with concentrations of ~2,600–2,800 ppm (Fig. 1b). In contrast to Pb^{2+}, Co^{2+} treatments yielded substantially lower precipitate masses than the control, with values of ~0.78–0.81 g at T1 and T2 and a further decrease to ~0.57 g at T3 (Fig. 1c). Despite the reduced solid yield, Co removal efficiencies remained high (97–98%) across all treatments, with no systematic decrease with increasing metal concentration (Fig. 1d).

By contrast, Cr^{3+}-amended systems exhibited lower pH values (≈7.5–7.8) than those observed for Pb^{2+} and Co^{2+}. Values remained around 7.8 at T1 and T2 and decreased to ~7.5 at the highest loading (T3) (Fig. 1a). Ammonium concentrations were markedly reduced (~2,000–2,450 ppm) and declined systematically from T1 to T3 (Fig. 1b). This was accompanied by a reduction in precipitate mass, which remained comparable to the control at T1 and T2 (~1.77–1.81 g) before dropping sharply to ~0.5 g at T3 (Fig. 1c). Despite the reduced solid yield, Cr removal remained relatively high (87–97%), although a clear decrease was observed at the highest loading (Fig. 1d).

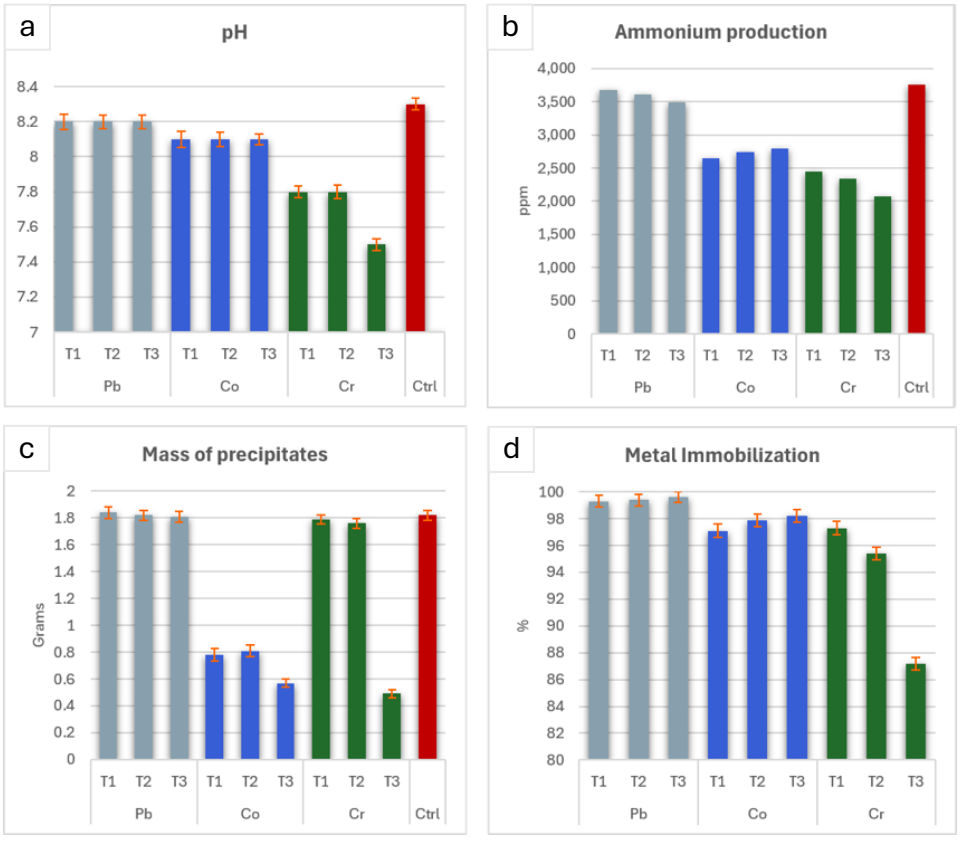

Figure 1. pH (a), ammonium production (b), mass of precipitates (c) and metal immobilisation efficiency (d) measured in crude-enzyme-driven EICP experiments with Pb, Co and Cr at three concentrations (T1–T3), compared with a metal-free control (Ctrl). Values represent mean ± SD (n = 3), except ammonium.

3.2. Microstructural analysis of precipitates (SEM)

SEM microstructural analyses were performed on powder samples mounted directly onto coated stubs, rather than on polished sections. This approach preserves the native external morphologies of the EICP precipitates and enables clear observation of surface textures and growth features, although aggregates appear in random orientations and may expose only parts of their internal structure. Even so, it provides high-fidelity access to the outer microstructures that characterise each metal treatment. The following subsections describe the principal morphologies observed for Pb, Co and Cr across treatments T1, T2 and T3.

3.2.1. Lead

Pb-treated samples (T1–T3) are dominated by large composite aggregates, typically 40–100 μm in diameter, which constitute the prevailing morphological class across all treatments (Fig. 2 Pb-T1, Pb-T2 and Pb-T3). These aggregates are heterogeneous and comprise multiple intergrown morphotypes rather than a single uniform habit. Common components include truncated sunflower-like structures with shallow central depressions (Fig. 2 Pb-A, Pb-C), aggregates of spheres and tabular to platy crystals forming locally grouped domains (Fig. 2 Pb-T1, Pb-T2 and Pb-B).

A prominent feature of the Pb system is the occurrence of dense aggregates composed of tightly packed spherical sub-units (Fig. 2 Pb-T2 and Pb-D). These spheroidal clusters are especially abundant and well organised at intermediate Pb loading (T2), forming multi-sphere assemblages. The surfaces of individual spheres are not uniform, ranging from smooth and compact to finely roughened, nanoparticulate or locally pitted textures, suggesting variable growth and coalescence histories. Individual spheres commonly display shared boundaries and partial fusion (Fig. 2 Pb-T2 and Pb-D). At lower Pb concentration (Pb-T1), spheroidal units are present but are less consistently organised and more commonly occur embedded within heterogeneous cauliflower-like aggregates; at the highest loading (Pb-T3), spheroidal textures are less regularly expressed and are accompanied by more fragmented and irregular composite masses.

In addition to the $CaCO_3$-dominated aggregates, Pb-treated samples contain several morphologies attributed to cerussite. These include fan-like (petaloid) bladed aggregates composed of broad, flattened blades radiating asymmetrically from a central core, observed in T3 (Fig. 2 Pb-E); spherical, raspberry-like globules (typically 2–10 μm in diameter) composed of densely packed nano- to submicron crystallites; and compact clusters of short, robust prismatic crystals forming blocky intergrown aggregates, observed in T2 and T3.

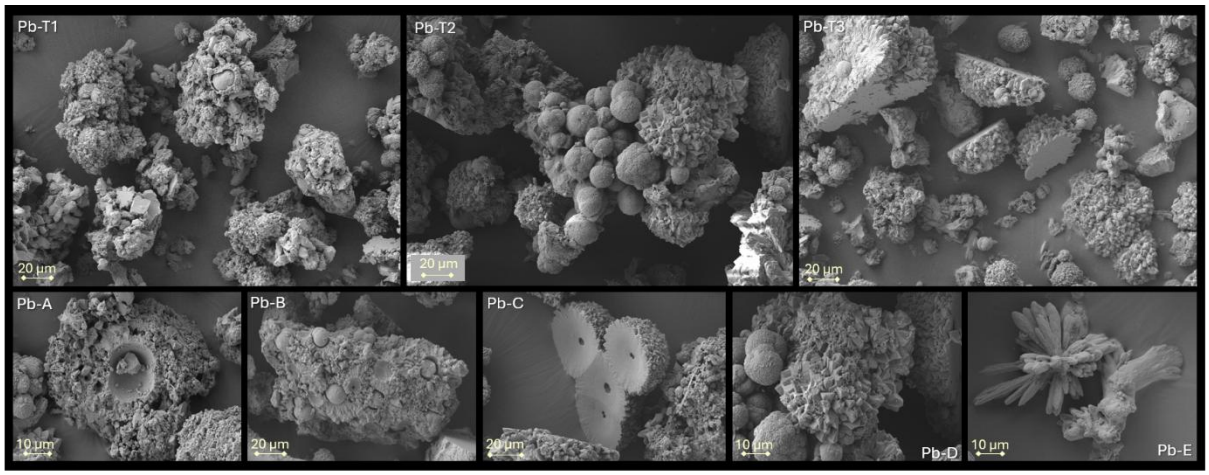

Figure 2. Lead-treated EICP precipitates across treatments (T1–T3) and representative morphologies (Pb-A to Pb-E). SEM images show the dominant Pb-bearing carbonate assemblages formed under increasing Pb loadings. Panels Pb-T1 to Pb-T3 illustrate the progression from loosely aggregated, cauliflower-like clusters (T1) to more compact spheroidal aggregates and botryoidal masses (T2), culminating in heavily fused, irregularly textured precipitates at the highest Pb concentration (T3). Panels Pb-A to Pb-E highlight characteristic morphologies observed throughout the system, including shallow sunflower-like structures with poorly developed radial organisation (Pb-A, C), botryoidal and nanoparticulate coatings (Pb-B), dense agglomerates with coalesced spheroidal sub-units and coarse surface textures (Pb-D), and asymmetric petaloid aggregates indicative of cerussite (Pb-E). Together, these images illustrate the tendency of Pb^{2+} to disrupt calcite growth, promoting highly aggregated, texturally heterogeneous precipitates across all treatments.

3.2.2. Cobalt

Co-treated samples (T1–T3) exhibit a range of composite precipitate morphologies that vary systematically with treatment level. At T1, the precipitated solids are dominated by irregular composite aggregates, typically ranging from ~20 to 80 µm. At low magnification, these aggregates appear as compact, cauliflower-like masses composed of multiple coalesced sub-units, with domed to lobate outlines and abundant lateral growths. Their surfaces are heterogeneous and micro-roughened, with pervasive fine-scale textural relief (Fig. 3 Co-T1, Co-B). Aggregates of smooth-surfaced spherical crystals also occur locally (Fig. 3 Co-A).

At T2, the precipitated solids are dominated by porous aggregates and sunflower-like morphotypes, commonly forming clustered assemblages (Fig. 3 Co-T2). The porous aggregates comprise well-defined pyramidal to spherical crystal units with open surface architectures, whereas the sunflower-like forms consist of compact radial units with short outward-projecting elements (petal-like) arranged around a central core. The two morphotypes frequently occur in close spatial association, with sunflower-like aggregates commonly attached to, or intergrown with, the surfaces of the porous aggregates, and grouped into composite clusters (Fig. 3 Co-T2).

At T3, the precipitates are characterised by a finer overall granulometry, forming aggregates of spheres with variable surface textures that are commonly associated with a continuous mass and occur as dispersed block-like composites (Fig. 3 Co-T3). The spherical units show heterogeneous surface expression, ranging from roughened coatings to more compact, irregular textures (Fig. 3 Co-D), and are frequently embedded

within or partially fused to the surrounding matrix, producing fragmented but cohesive aggregate blocks (Fig. 3 Co-T3, Co-E).

A distinctive microstructural feature of the Co-treated systems is the intricate, lace-like nanostructure mantling some of the aggregates, best developed at T2 but observed incipiently at T1 and T3 (Fig. 3 Co-F). At high magnification, the surfaces resolve into tessellated networks of tightly interwoven triangular micro-modules with pyramidal to spherical terminations, each composed of short plate-like crystallites diverging from a central axis and overlapping at slight angular offsets (Fig. 3 Co-G, H).

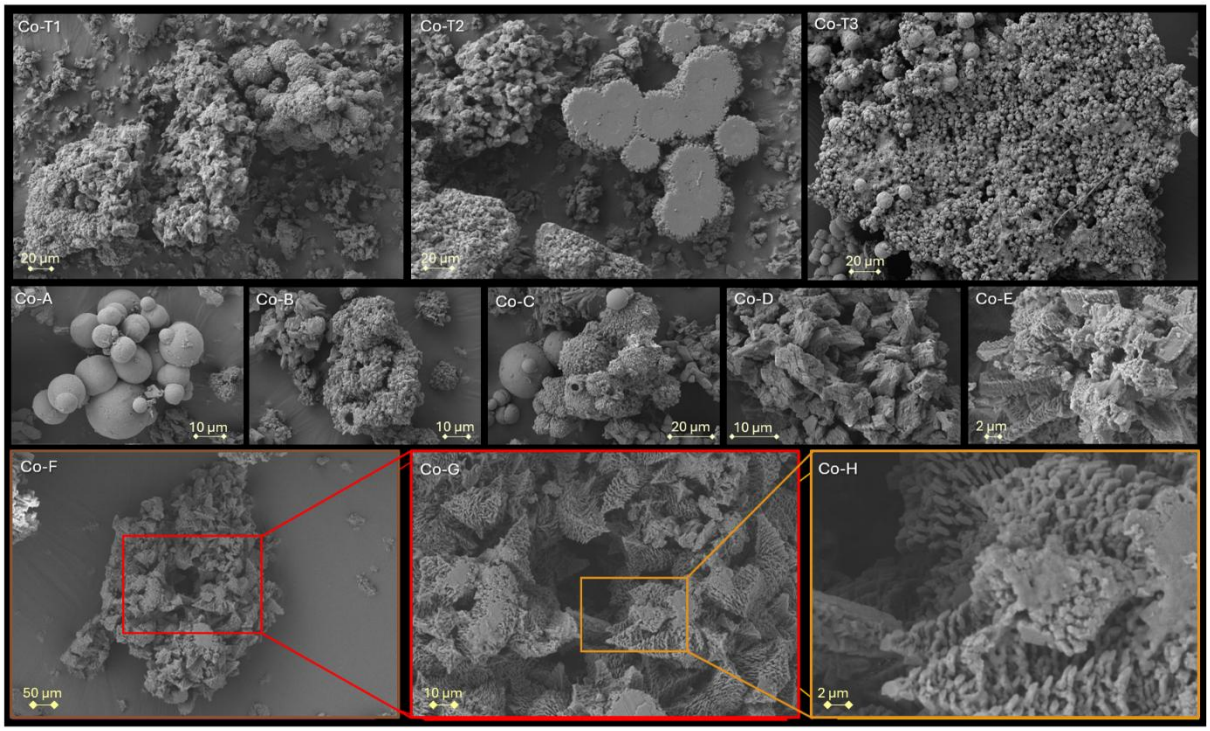

Figure 3. SEM images of cobalt-treated EICP precipitates across treatment levels (T1–T3), showing representative morphotypes and hierarchical structural detail. Top row (Co-T1 to Co-T3): dominant aggregate types at each treatment level, ranging from compact cauliflower-like composite aggregates (Co-T1) to clustered porous and sunflower-like morphotypes (Co-T2) and finer, densely fused spheroidal masses (Co-T3). Middle row: representative morphotypes, including smooth-surfaced spherical crystals (Co-A), cauliflower-like composite aggregates (Co-B), spherical and composite aggregates in close spatial association (Co-C), blocky intergrown crystals (Co-D), and serrated crystal clusters partially fused to the surrounding matrix (Co-E). Bottom row (Co-F, with sequential magnifications Co-G and Co-H): hierarchical organisation of the lace-like nanostructure, resolving into tessellated networks of tightly interwoven triangular micro-modules with pyramidal to spherical terminations, composed of short plate-like crystallites.

3.2.3. Chromium

Cr-treated samples display a clear evolution in precipitate morphology with increasing Cr concentration. At T1 (Fig. 4 Cr-T1), the precipitates are dominated by compact blocky aggregates, typically 10–70 µm in diameter, composed of intergrown microcrystals with well-defined faces and sharply delineated aggregate margins. At T2 (Fig. 4 Cr-T2), similar blocky aggregates coexist with spherical to sub-spheroidal clusters, reflecting the onset of morphological diversification. Radial morphologies are common,

including sunflower-like particles characterised by broadly circular outlines, shallow central depressions, and rims constructed from densely packed angular sub-units (Fig. 4 Cr-B, Cr-C). These radial forms occur both as discrete particles and as components embedded within larger composite aggregates.

At T3 (Fig. 4 Cr-T3, Cr-D, Cr-E), the precipitate morphology changes markedly. The assemblage is characterised by a fine-grained matrix composed of abundant spheroidal particles and short prismatic crystallites closely resembling the morphologies of the carbonate-rich aggregates observed at lower Cr loadings. Within this matrix, abundant elongated prismatic crystals occur as long, straight to slightly irregular blades and plates, commonly tens of micrometres in length, forming dense, interwoven mats. The compact aggregates characteristic of lower Cr loadings are no longer observed as discrete particles but instead persist as relict cores or substrates incorporated within the fine-grained matrix and associated prismatic crystal assemblage.

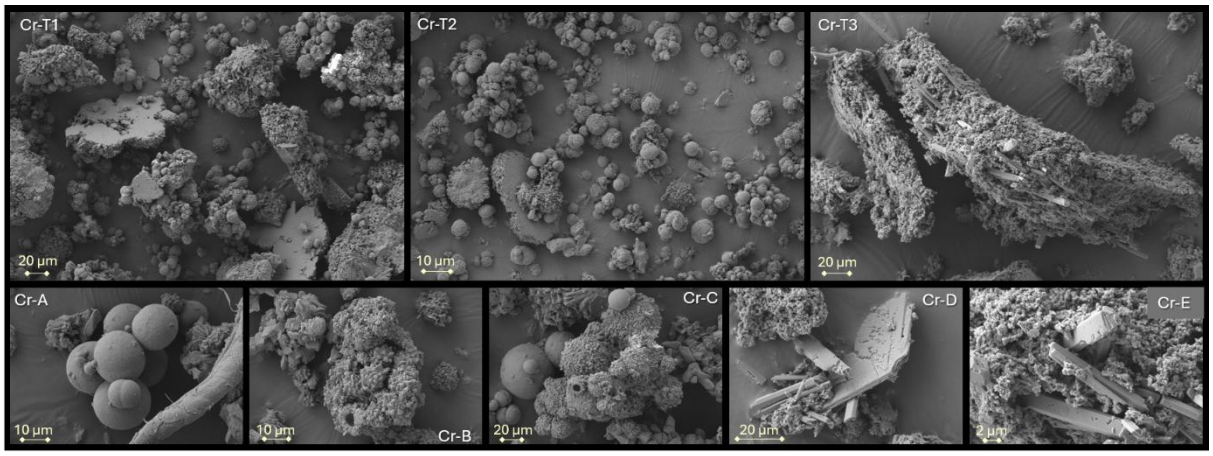

Figure 4. SEM images of Cr-treated EICP precipitates across increasing Cr concentrations (Cr-T1–T3) and representative Cr-associated morphologies (Cr-A to Cr-E). Cr-A shows spheroidal morphotypes commonly observed in T1 and T2. Cr-B and Cr-C illustrate sunflower-like particles and porous, cavernous aggregate textures characteristic of low to intermediate Cr loadings. Cr-D and Cr-E highlight the abrupt transition toward elongated prismatic morphologies that dominate at T3.

3.2.4. Description of the sunflower-like carbonate texture

Sunflower-like carbonate aggregates recur across all Pb- and Co-treated systems and at low to intermediate Cr loadings (Cr-T1, Cr-T2), albeit in variable abundance. Their persistence across three metals with divergent mineralogical outcomes provides a shared morphological baseline against which metal-specific partitioning, zoning and phase segregation can be evaluated. The texture is here named by analogy with the capitulum (inflorescence) of *Helianthus*, in which a central field of densely packed disk florets is surrounded by a peripheral ring of elongate ray florets; the analogy is strictly morphological and implies no structural homology or shared organising mechanism. Each aggregate is defined by a broadly circular to sub-circular outline, a central region occupying the position of the disk-floret field, and a peripheral rim of radially organised

crystalline sub-units, the ray-floret analogue, producing a rosette-like architecture (Fig. 5 Sf-1, Sf-2, Sf-4, Sf-5, Sf-7, Sf-8, Sf-9).

Individual aggregates range from a few to a few tens of micrometres and occur both as discrete particles and as components embedded within larger composites. The central region is usually denser and more compact than the outer rim, which is defined by outward-projecting elements that impart the radial organisation. The radial rim is constructed from discrete angular microcrystalline elements rather than continuous coatings; its sub-units vary in thickness, length and separation with metal treatment and concentration, being short and blocky in some particles and elongated, blade- to plate-like in others, but consistently preserving a centre-to-periphery arrangement.

The central architecture is consistent with a progressive sequence rather than a set of discrete forms: a spheroidal central core that becomes separated from the surrounding radial framework, leaving an open central cavity in its place. The simultaneous occurrence of core-filled centres, partially separated cores, and empty central cavities within the same aggregate population provides strong morphological evidence for a single detachment sequence. In its earliest expression, the spheroidal core is preserved in situ as a compact, smooth to finely textured body from which radial sub-units extend outward, locally bounded by an incipient annular separation (Fig. 5 Sf-8). At intermediate stages, the core remains only partially seated within its central cavity, displaced but still associated with the radial structure (Fig. 5 Sf-7), locally preserving a spiral to reniform trace reminiscent of capitulum phyllotaxis. Where separation is complete, the core is absent, leaving an open central cavity with sharply defined margins surrounded by the radial framework (Fig. 5 Sf-1, Sf-2, Sf-4, Sf-5, Sf-9); the floor of the cavity ranges from smooth and continuous to regularly pitted, with a dimpled surface texture (Fig. 5 Sf-2, Sf-5).

Sunflower-like aggregates coexist with spheroidal aggregates, blocky polyhedral clusters and prismatic crystals, and are commonly intergrown with or partially overgrown by these forms. Preservation ranges from well-defined, symmetric structures to disrupted variants in which the radial organisation is incomplete or locally obscured.

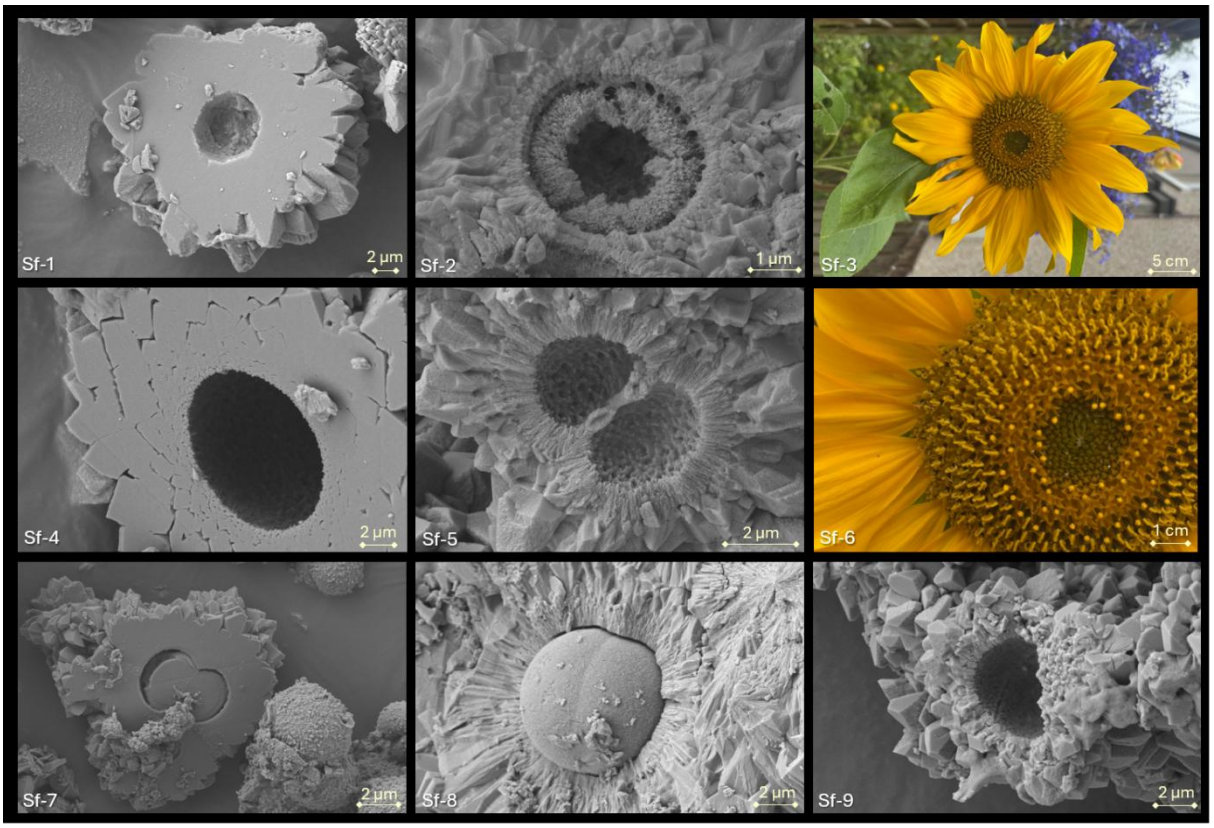

Figure 5. Sunflower-like carbonate morphologies formed during metal-doped EICP, shown alongside natural sunflower (*Helianthus annuus*) reference patterns (Sf-3, Sf-6). Panels Sf-1, Sf-2, Sf-4, Sf-5 and Sf-7–Sf-9 show representative SEM images of radial carbonate aggregates produced under Pb-, Co- and Cr-treatments. These structures are characterised by a central depression surrounded by outward-radiating crystallites, producing a rosette or "sunflower-like" habit. Pb-rich aggregates (Sf-1, Sf-2, Sf-4) exhibit broader, blocky petals and well-defined central voids, whereas Co-rich structures (Sf-5, Sf-7) display finer, densely packed radial blades and more pronounced textural organisation. Sf-9 illustrates the same rosette habit at low Cr loading (Cr-T1). Sf-7 and Sf-8 show the sunflower pattern with the central nucleus preserved *in situ*. Photographs of *Helianthus annuus* were taken by the author and are reproduced here for morphological comparison.

3.3. Crystalline phase assemblages and phase evolution (PXRD and Rietveld refinement)

Powder X-ray diffraction (PXRD) was used to identify the crystalline phase assemblages associated with the morphologically distinct carbonate precipitates formed under Pb-, Co- and Cr-amended EICP conditions. As no internal standard was employed, phase proportions derived from Rietveld refinement are semi-quantitative and are used here to support comparative mineralogical trends across treatments rather than absolute quantification; proportions were normalised to 100 wt% (Table 1). Throughout, the substitution classes reported for each metal represent refinement constructs (see Section 2.6) used to capture lattice distortion and compositional heterogeneity rather than true bulk solid-solution compositions. More generally, removal of a metal from solution (Section 3.1) and its incorporation into the recovered crystalline phases are distinct quantities and are not equated in what follows: the diffraction, chemical and spatial analyses reported here resolve the identity, association and relative

proportions of the phases present, not a closed elemental mass balance for each metal within the solids. A fraction of the removed metal may therefore reside in hosts not fully constrained by these methods, including surface-adsorbed, organically complexed, or poorly ordered or amorphous material, whose quantitative apportionment lies beyond the scope of the present study.

Pb-treated samples exhibited a concentration-dependent evolution in crystalline phase assemblages. At the lowest Pb concentration (T1), diffraction patterns were dominated by calcite (86.4 wt%), accompanied by calcite-type components modelled across the apparent substitution classes, comprising 7.3 wt% in the ≤5% class, 5.4 wt% in the 5–10% class, and 0.8 wt% in the 10–15% class. Discrete Pb carbonate phases were detected below 0.1%. At the intermediate Pb concentration (T2), calcite remained the principal phase (71.5 wt%), while calcite-type components modelled across the apparent substitution classes accounted for 13.3 wt%, 8.1 wt%, and 4.1 wt% in the ≤5%, 5–10%, and 10–15% classes, respectively. Cerussite ($PbCO_3$) was identified at this stage, accounting for 3.1 wt% of the crystalline assemblage. At the highest Pb concentration (T3), calcite accounted for 67.7 wt%, whereas calcite-type components modelled across the apparent substitution classes comprised 11.6 wt%, 9.3 wt%, and 5.2 wt% in the ≤5%, 5–10%, and 10–15% classes, respectively. Cerussite increased from 3.1 wt% at T2 to 6.2 wt% at T3 (Fig. 6).

At the lowest Co concentration (T1), the mineral assemblage comprised 27.9 wt% calcite together with 72.1 wt% of a calcite-type component modelled in the ≤5% Co apparent-substitution class. At the intermediate Co concentration (T2), calcite increased to 36.2 wt%, accompanied by 63.8 wt% of the ≤5% Co apparent-substitution class, while no meaningful contributions from the higher apparent-substitution classes were detected. At the highest Co loading (T3), calcite increased further to 46.4 wt%, whereas the ≤5% Co apparent-substitution class decreased to 53.6 wt%. Throughout the Co series, contributions from the 5–10% and 10–15% Co apparent-substitution classes remained below the detection threshold (<0.1 wt%), and no discrete Co-bearing crystalline phases were identified. Calcite and the ≤5% Co apparent-substitution class together accounted for essentially the entire refined crystalline assemblage (Fig. 6).

At low and intermediate Cr loadings (T1 and T2), the crystalline assemblage comprised 98.3 wt% and 98.6 wt% calcite, respectively, together with 1.7 wt% and 1.4 wt% of the ≤5% Cr apparent-substitution class. No discrete Cr-bearing crystalline phases were identified (Fig. 6). At the highest Cr loading (T3), morphologically distinct aggregated phases were observed by SEM; however, the recovered mass (~0.5 g) was insufficient to fully pack the sample holder used in our configuration and reduced-volume mounting yielded diffraction patterns of insufficient intensity for reliable phase identification or quantitative Rietveld refinement. Consequently, Cr-T3 is not included in Table 1.

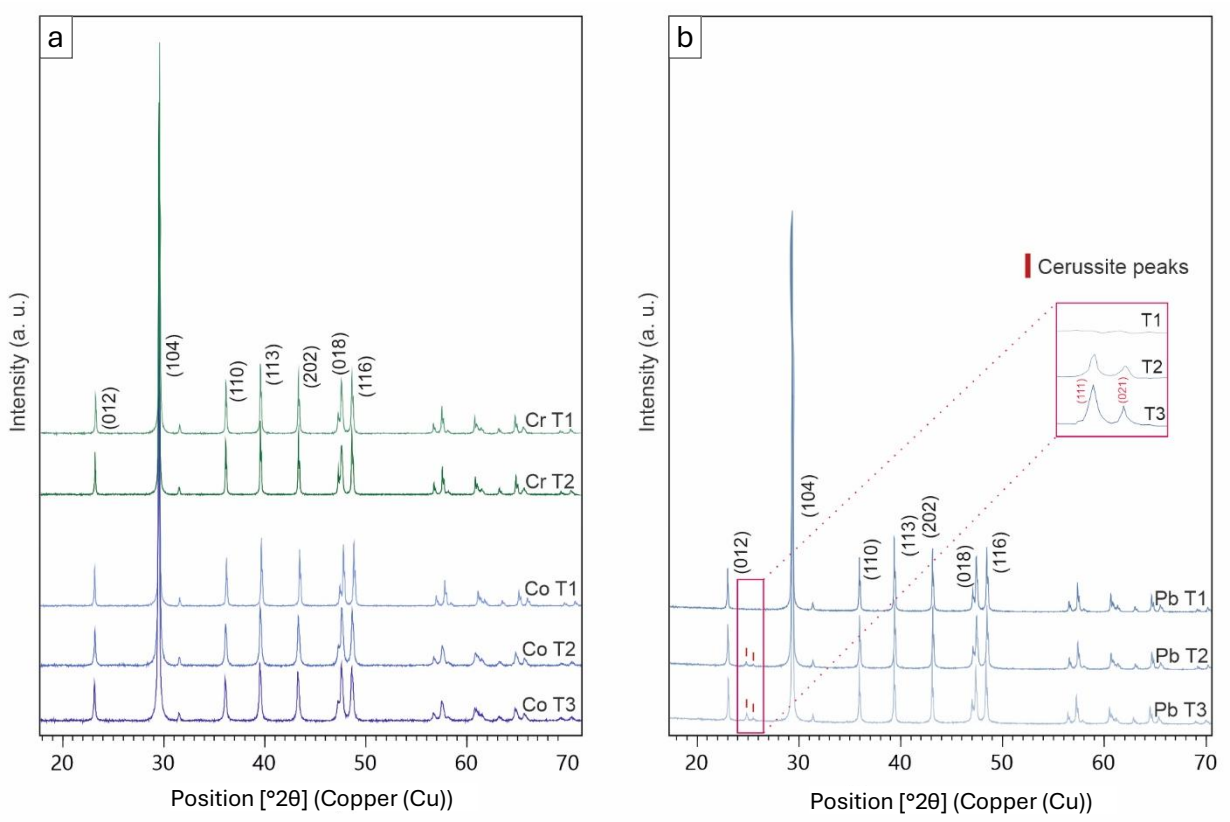

Figure 6. Stacked PXRD patterns of Co-, Cr- and Pb-treated samples. Patterns are vertically offset and normalised for visual comparison. In the Pb system (b), discrete cerussite reflections emerge at T2 and intensify at T3 (inset), whereas in (a), Co-treated samples remain calcite-dominated across all concentrations (T1–T3) and Cr-treated samples remain calcite-dominated at T1 and T2.

Table 1. Semi-quantitative phase proportions (wt%) from Rietveld refinement of PXRD data for Pb- and Co-treated samples (T1–T3) and Cr-treated samples (T1–T2).

Metal	Treatment	Calcite	Metal-substituted calcite (≤5%)*	Metal-substituted calcite (5–10%)*	Metal-substituted calcite (10–15%)*	Metal carbonate phases (e.g. cerussite)	Total
Pb	T1	86.4	7.3	5.4	0.8	<0.1	100.0
	T2	71.5	13.3	8.1	4.1	3.1	100.0
	T3	67.7	11.6	9.3	5.2	6.2	100.0
Co	T1	27.9	72.1	<0.1	<0.1	N.A.	100.0
	T2	36.2	63.8	<0.1	<0.1	N.A.	100.0
	T3	46.4	53.6	<0.1	<0.1	N.A.	100.0
Cr	T1	98.3	1.7	<0.1	N.A.	N.A.	100.0
	T2	98.6	1.4	<0.1	N.A.	N.A.	100.0

Phase proportions were normalised to 100 wt%.
Values below 0.1 wt% are reported as <0.1 and treated as zero in the normalisation.
N.A. indicates that the phase or apparent substitution class was not detected (0 wt%) in that system.
*Apparent substitution classes correspond to refinement models used for fitting lattice distortion and should not be interpreted as measured bulk metal occupancies.

3.4. Chemical composition and spatial partitioning of metals (SEM–EDS and nano-XRF mapping)

Semi-quantitative SEM–EDS analyses and synchrotron nano-XRF mapping were used to characterise the chemical identity and spatial distribution of Pb-, Co- and Cr-bearing phases within the EICP precipitates. Representative semi-quantitative compositional data for all treatments are provided in the Supplementary Materials. Owing to matrix effects and multiphase interaction volumes, EDS data are interpreted comparatively rather than as fully quantitative measurements, with emphasis placed on relative metal enrichment, co-association with Ca, and the presence or absence of anion signatures (C, S) indicative of carbonate, sulphate or hydroxide phases. Nano-XRF maps complement these spot analyses by revealing whether metal distributions are homogeneous or heterogeneous at the 2–5 µm scale. Synchrotron nano-XRF mapping was performed for Pb- and Co-bearing samples; Cr-bearing samples were not mapped owing to beamtime limitations, and their mineralogy was instead evaluated by SEM morphology and semi-quantitative EDS, combined with the PXRD data available for T1 and T2.

3.4.1. Lead: distribution between Pb-substituted $CaCO_3$ and discrete Pb-carbonate phases

For descriptive purposes, Pb-bearing carbonate analyses were grouped into four compositional categories according to Pb concentrations measured by SEM–EDS: slightly Pb-enriched (<5 wt% Pb), moderately Pb-enriched (5–30 wt% Pb), Pb-rich (>30 wt% Pb), and cerussite. In T1, the analysed carbonate domains were slightly to moderately Pb-enriched, with Pb concentrations ranging from 1.35 to 11.01 wt%. In T2, most analysed domains were moderately Pb-enriched, although isolated Pb-rich compositions exceeding 30 wt% Pb were also recorded. In T3, moderately Pb-enriched rims, Pb-rich central domains, and discrete cerussite particles were identified. Representative SEM–EDS analyses are reported in Table S4.1 (Supplementary Material).

Backscattered electron images of the T3 precipitates show bright, high-Z domains distributed within a darker Ca-rich matrix (Fig. 7a). Binary segmentation of these regions shows that they account for approximately 6–7% of the analysed area and occur as spatially discrete domains throughout the field of view (Fig. 7b).

Across all three treatments, the highest Pb concentrations were consistently measured in the central regions of the carbonate aggregates, whereas lower Pb concentrations were recorded towards their rims. In T1, Pb concentrations in the core and intermediate regions ranged from 5.34 to 11.01 wt%, while rim analyses yielded 1.35–7.57 wt% Pb. In T2, the central and intermediate regions contained 18.34–31.57 wt% Pb, whereas rim analyses yielded 12.82–13.93 wt% Pb. In T3, Pb-rich central domains contained 30.03–35.50 wt% Pb, while moderately Pb-enriched rims contained 8.69–13.94 wt% Pb. Cerussite compositions of 56.80–57.40 wt% Pb were measured in the centres of the petal-like crystals shown in Fig. 8g.

SEM–EDS elemental maps show spatial variations in Pb and Ca distribution across the T1, T2 and T3 precipitates (Fig. 8a to g). Higher-magnification SEM–EDS maps of T3 aggregates show stronger Pb signals in their central regions and weaker signals towards their outer margins (Fig. 8e, f). The synchrotron Nano-XRF map displays the same spatial pattern, with Pb-enriched central regions surrounded by comparatively Pb-depleted outer regions (Fig. 8h).

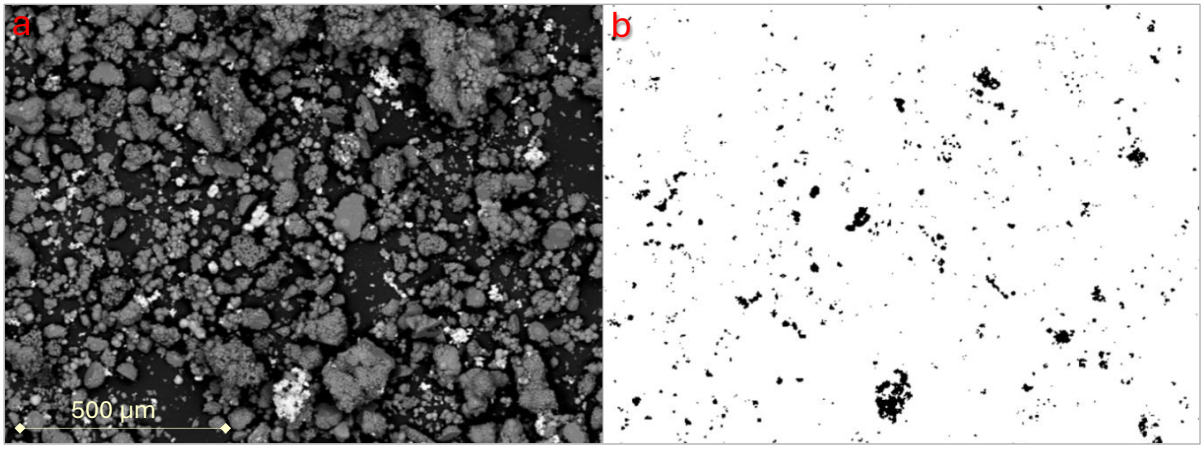

Figure 7. Backscattered electron (BSE) image of Pb-treated (T3) EICP precipitates (a, left) and corresponding binary segmentation mask of high-Z regions (b, right). In the BSE image (a), brighter domains represent Pb-rich carbonate phases (cerussite) dispersed within a $CaCO_3$-dominated matrix. In the segmented image (b), these Pb-rich domains are represented in dark, highlighting their spatial distribution and accounting for approximately 6–7% of the analysed area.

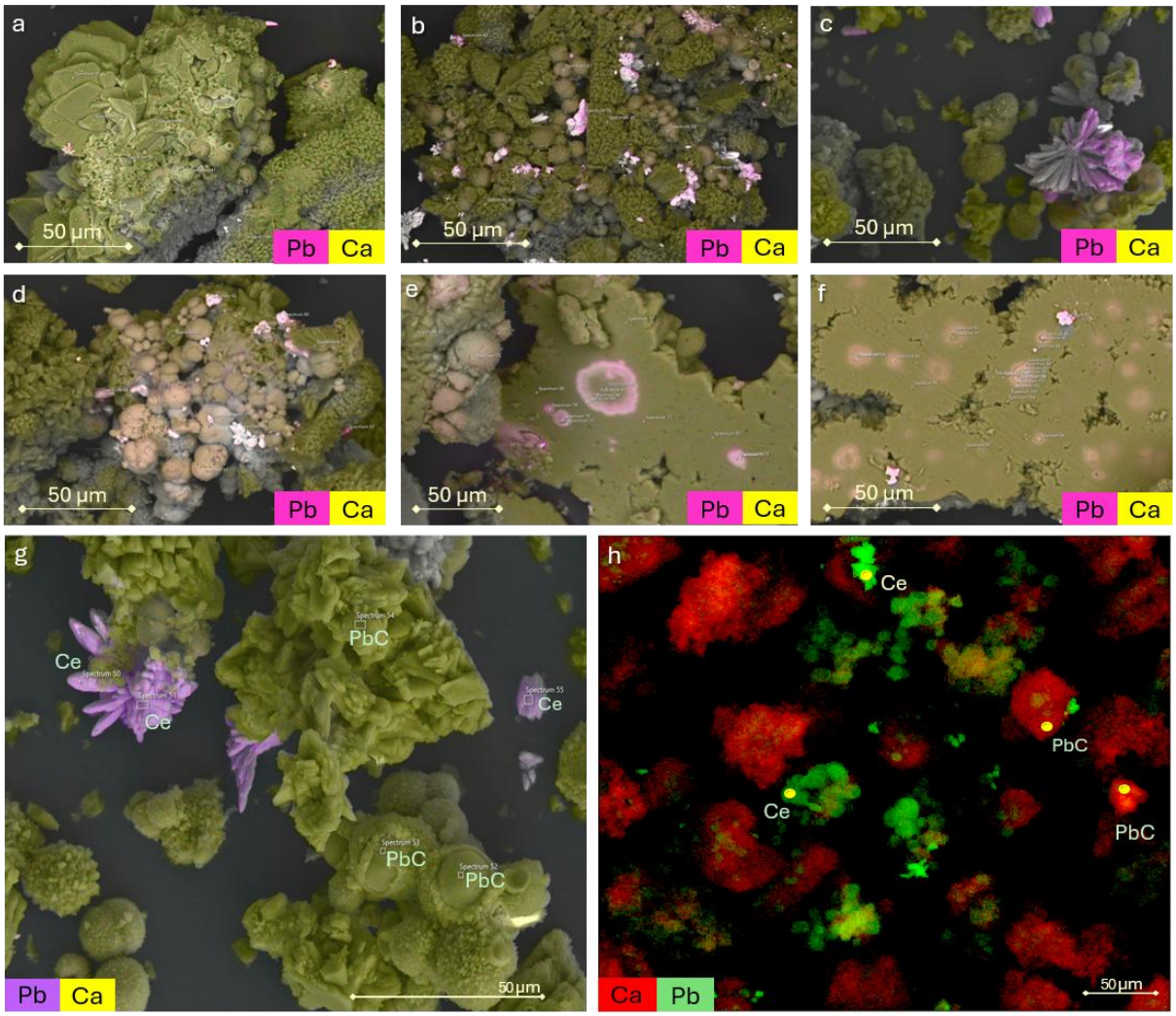

Figure 8. SEM–EDS (a–g) and synchrotron Nano-XRF (h) characterisation of Pb-treated EICP precipitates. SEM–EDS elemental maps of T1 (a), T2 (b) and T3 (c) precipitates showing the distributions of Pb and Ca. d) Representative spherical carbonate aggregate from T3. e–f) Higher-magnification SEM–EDS images showing internal compositional heterogeneity within carbonate aggregates. g) SEM–EDS image showing particles identified as cerussite (Ce) and Pb-rich carbonate domains (PbC). h) Synchrotron Nano-XRF elemental map showing the distributions of Pb and Ca within representative Pb-treated precipitates in T3.

3.4.2. Cobalt: composition and spatial distribution within carbonate precipitates

For descriptive purposes, Co-bearing carbonate analyses were grouped into three compositional categories according to Co concentrations measured by SEM–EDS: slightly Co-enriched (<0.5 wt% Co), moderately Co-enriched (0.5–1.5 wt% Co), and Co-rich (>1.5 wt% Co). Representative SEM–EDS analyses are reported in Table S4.2 (Supplementary Material).

In T1, all analysed carbonate domains were classified as slightly Co-enriched, with Co concentrations ranging from 0.11 to 0.39 wt%. In T2, all analysed domains were moderately Co-enriched, with Co concentrations ranging from 0.54 to 0.91 wt%. In T3, Co concentrations ranged from 1.10 to 4.34 wt%, comprising both moderately Co-enriched and Co-rich domains.

SEM–EDS spot analyses show Co distributed throughout the carbonate aggregates in all three treatments, with measurable Co concentrations recorded in both central and peripheral regions of the particles. Local variations in Co concentration were observed within individual aggregates, but no systematic spatial concentration pattern was identified.

SEM–EDS elemental maps show Co distributed across the carbonate aggregates in T1, T2 and T3 (Fig. 9a–d). Synchrotron Nano-XRF maps show a comparable spatial distribution, with Co detected throughout the analysed aggregates and exhibiting local variations in signal intensity. The principal Co-bearing features identified in the Nano-XRF maps spatially coincide with the Ca-bearing aggregates (Fig. 9e–g).

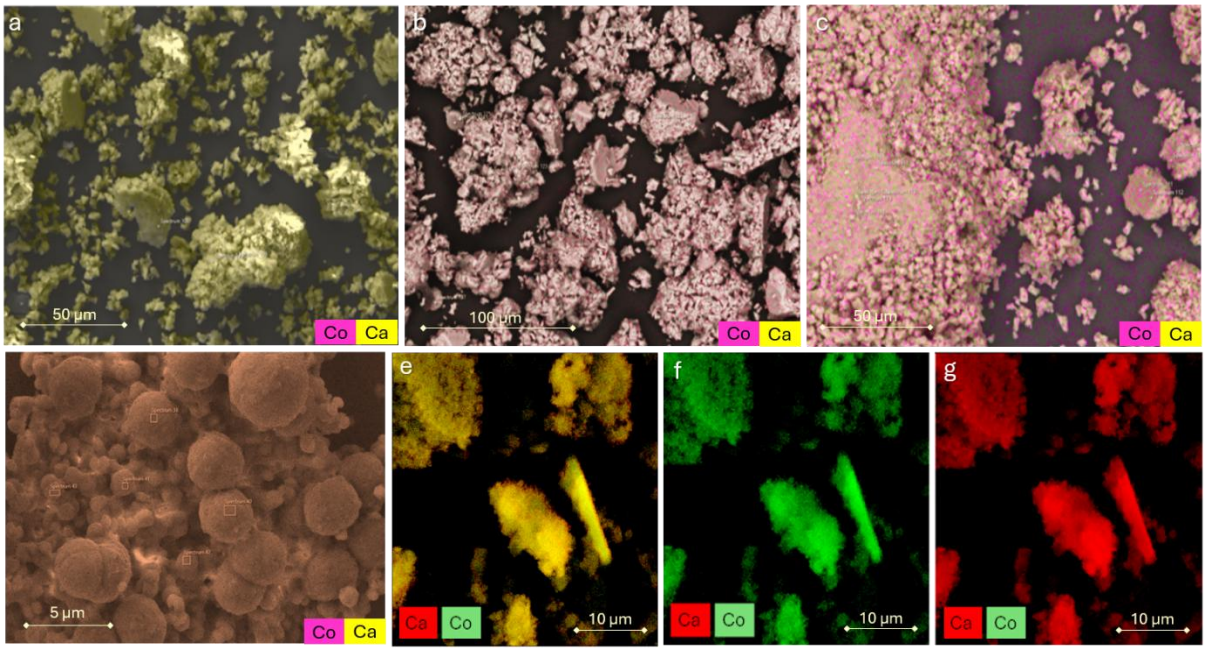

Figure 9. SEM–EDS (a–d) and synchrotron Nano-XRF (e–g) images of Co-treated EICP precipitates. (a–c) SEM–EDS elemental maps of T1, T2 and T3, respectively, showing the distributions of Co and Ca. (d) Representative SEM image of carbonate aggregates from T3. (e–g) Synchrotron Nano-XRF maps of T3 showing the combined Ca–Co distribution (e), Co distribution (f), and Ca distribution (g).

3.4.3. Chromium: composition and spatial distribution within precipitates

For descriptive purposes, Cr-bearing domains were grouped into three compositional categories according to Cr concentrations measured by SEM–EDS: slightly Cr-enriched (<2 wt% Cr), moderately Cr-enriched (2–5 wt% Cr), and highly Cr-enriched (>5 wt% Cr). Representative SEM–EDS analyses are reported in Tables S4.3 and S4.4 (Supplementary Material).

In T1, all analysed domains were classified as slightly Cr-enriched, with Cr concentrations ranging from 0.25 to 1.09 wt%. Calcium concentrations ranged between approximately 25 and 62 wt% in the analysed particles (Fig. 10 b). In T2, Cr concentrations ranged from 0.52 to 4.84 wt%, comprising both slightly and moderately Cr-enriched domains. Most analysed particles contained less than 5 wt% Cr (Fig. 10c, d).

In T3, Cr concentrations ranged from 1.42 to 10.47 wt%, comprising slightly, moderately and highly Cr-enriched domains (Fig. 10e–h). Alongside Ca-rich particles similar to those observed in T1 and T2, additional particles exhibiting higher Cr concentrations and lower Ca contents were identified.

SEM–EDS analyses also identified Ca–S-rich domains within the T3 precipitates (Table S4.4). These domains contained approximately 29–30 wt% Ca and 21–22 wt% S, together with minor Cr (0.15–1.35 wt%), and were associated with elongated prismatic and bladed crystals observed in the SEM images (Fig. 10f, h). In addition to the dominant Cr-bearing and Ca–S-rich compositions, minor non-target trace elements were locally detected within the Cr-treated precipitates. Isolated Ba-bearing particles were identified in association with the Ca–S-rich domains (Fig. 10g), with Ba concentrations ranging from 0.06 to 1.42 wt% (Table S4.5), whereas trace Cu was detected only in a small number of analyses from the Cr-treated precipitates, with concentrations ranging from 0.05 to 1.13 wt% (Table S4.5). Both elements were restricted to isolated microdomains and were not observed as pervasive constituents of the carbonate-rich precipitates.

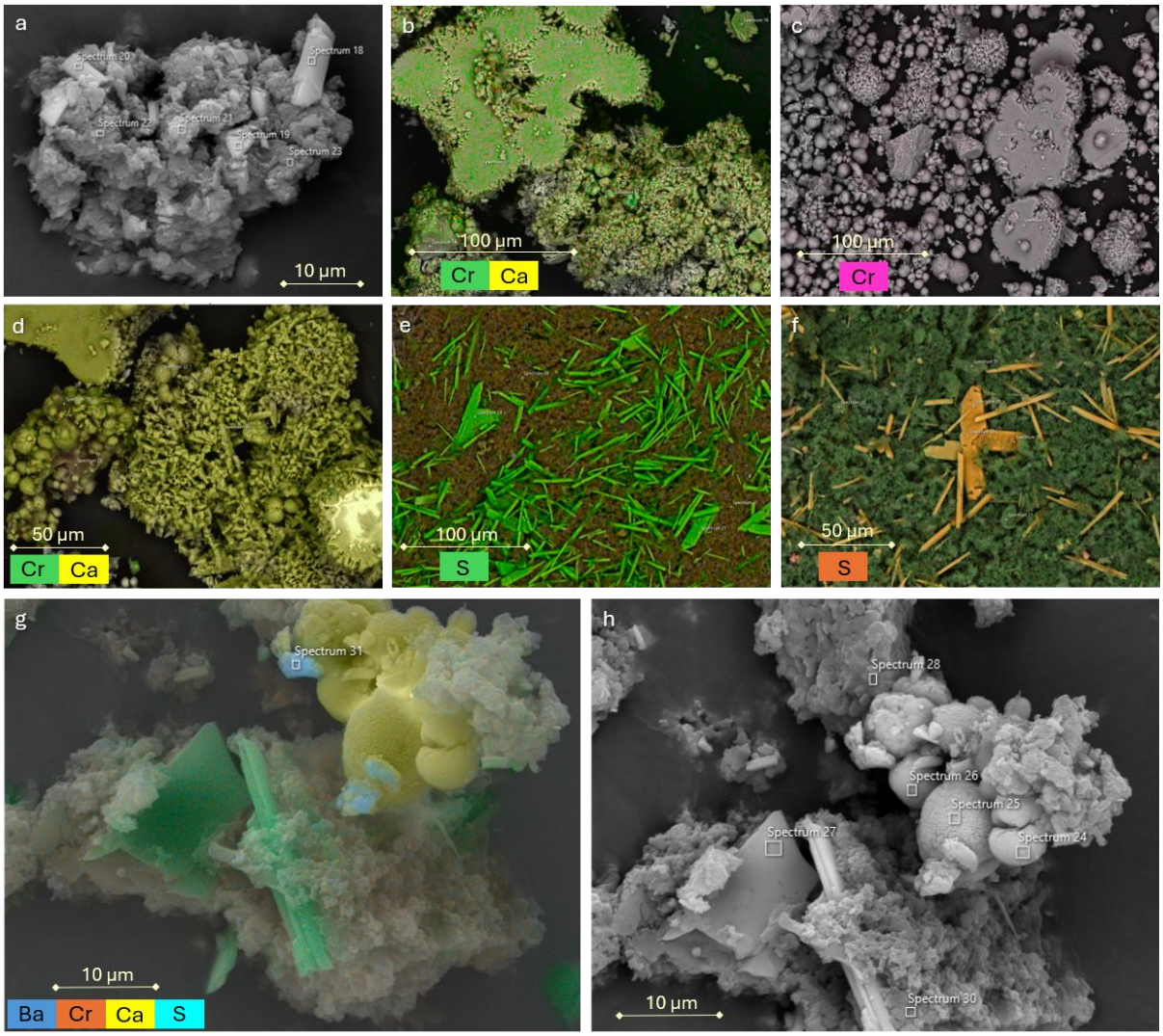

Figure 10. SEM and SEM–EDS characterisation of chromium-treated EICP precipitates. (b) Representative T1 precipitates showing Ca-rich carbonate particles with trace Cr. (c–d) Representative T2 precipitates illustrating increased Cr association within carbonate particles. (a, e–h) Representative T3 precipitates

showing the coexistence of carbonate-derived particles with chemically distinct Cr-rich, S-bearing and Ba-bearing domains, including prismatic and bladed morphologies. Spectrum labels correspond to the SEM–EDS analyses reported in the Supplementary Materials. Scale bars range from 10 to 100 μm.

4. Discussion

4.1. Metal-specific crystallogenetic pathways in crude-enzyme EICP

Under an identical crude-enzyme EICP protocol, Pb, Co and Cr followed distinct crystallogenetic pathways governed by differences in crystal-chemical compatibility, aqueous speciation and interactions with evolving carbonate supersaturation. Rather than reflecting a universal immobilisation mechanism, these observations demonstrate that metal chemistry primarily controls how carbonate precipitation pathways evolve, which mineral phases become stabilised, and the stage at which metal partitioning becomes effective.

Bulk metal removal efficiencies alone do not distinguish these mineralogical outcomes. Although Pb and Co were removed from solution with similarly high efficiencies, they were retained through fundamentally different mineralogical pathways, whereas Cr progressively disrupted carbonate biomineralisation, resulting in reduced carbonate production and lower overall removal. Resolving the mineralogical hosts responsible for immobilisation is therefore essential for understanding contaminant fate and the long-term stability of biomineralized products.

Increasing Pb loading promoted progressive mineralogical partitioning between Ca-bearing carbonate and discrete Pb-carbonate phases, representing the clearest concentration-dependent evolution observed among the three investigated metals. At low Pb loading, Pb was retained predominantly within $CaCO_3$-dominated biominerals, whereas higher Pb availability progressively favoured the stabilisation of compositionally distinct Pb-carbonate products alongside Ca-bearing carbonate. Rather than continued accommodation within a single calcite-type phase, increasing Pb loading shifted Pb retention towards mineralogical segregation into discrete carbonate phases.

This concentration-dependent evolution likely reflects the crystal-chemical constraints governing Pb incorporation during carbonate growth. Experimental and atomistic studies have demonstrated that Pb can substitute for Ca during calcite precipitation, although its relatively large ionic radius introduces local structural distortion that limits extensive lattice incorporation (Reeder, 1996; Sturchio et al., 1997). Likewise, Callagon et al. (2014) showed that Pb can be incorporated into near-surface layers of strained Pb-rich calcite during dissolution and epitaxial regrowth under circumneutral conditions, without precipitation of discrete cerussite. The present results are consistent with these observations while further indicating that increasing Pb availability progressively favours mineralogical partitioning into compositionally distinct Pb-carbonate phases under continuous biomineralisation.

Microanalytical observations provide direct evidence for this progressive evolution. At T1, Pb occurred predominantly at relatively low concentrations within Ca-rich carbonate domains (1.35–11.01 wt%). Increasing Pb availability generated

progressively more heterogeneous carbonate compositions at T2 (12.82–31.57 wt%), followed by systematic compositional zoning at T3, where crystal cores contained 30.03–35.50 wt% Pb and outer growth zones contained substantially lower concentrations (8.69–13.94 wt%). This zoning is consistent with preferential Pb incorporation during the earliest stages of carbonate growth. Under sustained Ca supply, continued carbonate precipitation would progressively decrease the Pb/Ca ratio of the mineralising solution, favouring the formation of increasingly Ca-rich outer growth zones.

At the highest Pb loading, discrete cerussite (56.8–57.4 wt% Pb) formed a compositionally distinct Pb-carbonate phase rather than representing the Pb-rich compositional extreme of the zoned Ca-bearing crystals. The absence of intermediate Pb compositions between the Pb-enriched carbonate domains and cerussite, together with the independent identification of cerussite by PXRD, supports this interpretation. Unlike acidic carbonate replacement systems, where calcite is progressively consumed through coupled dissolution–precipitation reactions that generate reaction fronts, porous textures and pseudomorphic replacement (Yuan et al., 2016, 2018; Kim et al., 2021, 2023), the crude-enzyme EICP system investigated here operated under fundamentally different geochemical conditions. Carbonate alkalinity was continuously generated through ureolysis while dissolved Ca remained available throughout biomineralisation, creating a precipitation-dominated environment rather than one governed by calcite dissolution. Consequently, calcite growth and cerussite precipitation proceeded concurrently, producing the coexistence of Ca-bearing carbonate and discrete Pb-carbonate phases instead of replacement of one mineral by another.

By contrast, Co exhibited consistently high immobilisation efficiencies (97–98%) across all investigated loadings without the development of a discrete crystalline Co-dominated phase. PXRD showed that the recovered crystalline assemblages remained $CaCO_3$-dominated throughout the series, with no detectable Co-carbonate or Co-hydroxide phase within the sensitivity of laboratory X-ray diffraction.

The Rietveld refinement results are fully consistent with the microanalytical observations, indicating that the recovered carbonate assemblages remained $CaCO_3$-dominated while Co was retained as a minor constituent of the calcite-type biominerals. The refinement classes should therefore be interpreted as modelling constructs that account for lattice distortion, crystallite-size effects and compositional heterogeneity within the calcite-type carbonate assemblage, rather than as direct measures of crystallographic Co occupancy. This behaviour is consistent with the strongly non-ideal nature of the $(Ca,Co)CO_3$ solid solution, which thermodynamically limits extensive Co incorporation into calcite (Katsikopoulos et al., 2008; González-López et al., 2014). Co uptake is further influenced by precipitation kinetics and crystallographically distinct growth sites (Lorens, 1981; Paquette & Reeder, 1995; Reeder, 1996). Experimental AFM observations have shown that Co^{2+} perturbs calcite step propagation, promoting local surface enrichment while inhibiting the continued advance of subsequent growth layers (Freij et al., 2004). This mechanism is consistent with the marked decoupling between carbonate production and metal removal observed in the present experiments. Whereas the control and Pb-treated systems produced approximately 1.80–1.84 g of precipitate,

Co-treated systems yielded only 0.78–0.81 g at T1–T2 and ~0.57 g at T3 while maintaining removal efficiencies of 97–98%. Together, these observations indicate that Co substantially modified carbonate nucleation and growth without preventing efficient transfer of dissolved Co into the recovered solids.

Previous studies have shown that Co interactions with calcite surfaces can promote heterogeneous nucleation and growth of secondary Co-bearing phases, although the formation and identity of Co-carbonate and Co-hydroxide products remain highly sensitive to solution chemistry and interfacial conditions (Xu et al., 2015; Riechers et al., 2022). Under the crude-enzyme EICP conditions investigated here, no discrete crystalline Co-bearing phase developed even at the highest investigated loading (20 mM). Instead, Co remained diffusely associated with the carbonate biominerals, indicating that efficient immobilisation was achieved through widespread association with the growing $CaCO_3$ matrix rather than mineralogical segregation into an independent Co phase. In contrast to Pb, where increasing loading progressively promoted cerussite stabilisation, Co remained distributed within the carbonate assemblage despite similarly high removal efficiencies, demonstrating that comparable bulk immobilisation can arise through fundamentally different crystallogenetic pathways.

Among the three investigated metals, Cr exerted the strongest inhibition of carbonate biomineralisation, defining the practical limit of the crude-enzyme EICP system investigated here. Unlike Pb and Co, which maintained consistently high immobilisation efficiencies despite following distinct crystallogenetic pathways, Cr was the only metal to exhibit a systematic decline in removal efficiency, decreasing from approximately 97% at T1 to ~87% at T3. This progressive decline was accompanied by reduced carbonate production, progressively lower final pH, lower ammonium concentrations indicative of greater inhibition of ureolysis, and the emergence of chemically distinct Cr-rich, Ca-depleted precipitates. Collectively, these observations indicate that increasing Cr loading progressively shifted immobilisation away from carbonate-controlled precipitation.

This behaviour is consistent with the poor crystal-chemical compatibility of Cr(III) with calcite together with its strong tendency towards hydrolysis and aqueous complexation under alkaline conditions (Rai et al., 2007; Fang et al., 2022). At low to intermediate Cr loadings, Cr remained only weakly associated with carbonate-rich assemblages, whereas increasing Cr availability progressively suppressed carbonate precipitation and promoted the development of chemically distinct Cr-rich domains. Although SEM–EDS does not permit definitive mineral identification, the systematic association of Cr with S-rich, Ca-depleted regions, together with the marked reduction in carbonate production and the disappearance of calcite-dominated microstructures, is consistent with immobilisation occurring predominantly within chemically distinct non-carbonate phases.

Microanalytical observations further resolve the compositional evolution accompanying this progressive diversion of mineralisation pathways. SEM–EDS revealed progressively increasing Cr enrichment, from generally <1.1 wt% at T1 to local concentrations exceeding 10 wt% at T3, while a second population of Ca- and S-rich precipitates

displaying gypsum-like morphology became increasingly abundant. These Ca–S-rich phases are consistent with a competing sulphate precipitation pathway that may have reduced Ca^{2+} availability for carbonate precipitation, thereby contributing further to suppression of carbonate biomineralisation. Sulphate supplied primarily by the $Cr_2(SO_4)_3$ reagent, and potentially also by the crude soybean extract, provides a plausible source for this competing precipitation pathway. Because insufficient precipitate was recovered from Cr-T3 for reliable PXRD refinement, interpretation at the highest loading necessarily relies primarily on SEM–EDS observations.

In contrast to Pb and Co, whose distinct crystallogenetic pathways nevertheless maintained efficient immobilisation, increasing Cr loading progressively compromised the biomineralisation process itself. Rather than simply altering the mineralogical host responsible for Cr retention, increasing Cr availability reduced carbonate formation and ultimately diminished overall immobilisation efficiency. It should also be recognised that, whereas Pb and Co were introduced as chloride salts, Cr was supplied as $Cr_2(SO_4)_3$. Consequently, the Cr system differed not only in metal chemistry but also in counter-ion composition, and the contribution of sulphate availability to the observed suppression of carbonate biomineralisation cannot be fully separated from the effects of Cr(III) hydrolysis under the present experimental design.

4.2. Incidental immobilisation of Copper and Barium

The altered geochemical environment established under high Cr loading also influenced the behaviour of non-target trace elements present in the experimental system. Copper, present as a trace component of the crude soybean extract used for enzyme preparation and therefore common to all treatments, was detected in the recovered precipitates only in the Cr-treated systems, with concentrations ranging from 0.05 to 1.13 wt%. As the crude soybean extract constituted the only source of Cu in the experimental system, its occurrence in the Cr-treated precipitates suggests preferential retention under the altered geochemical conditions generated by increasing Cr loading, although the mechanism responsible remains unresolved. In addition, isolated Ba-bearing particles containing 0.06–1.42 wt% Ba were associated with the Ca–S-rich domains of the Cr-T3 assemblage, consistent with a minor sulphate-bearing phase. Although these observations were not a primary objective of the present study, they further indicate that the sulphate-rich geochemical environment established under high Cr loading modified trace-element partitioning relative to the carbonate-dominated Pb and Co systems. Because Cu and Ba were identified only in a limited number of microanalyses, these observations are best regarded as ancillary evidence of altered trace-element partitioning rather than as evidence for a systematic multi-element co-immobilisation mechanism.

4.3. Sunflower-like textures as a shared morphological motif

Sunflower-like carbonate crystals recurred as a characteristic morphological motif throughout the crude-enzyme EICP products, irrespective of metal identity. They were observed across the Pb-, Co- and Cr-bearing systems, differing primarily in abundance and internal chemical architecture, and were absent only in the Cr-T3 treatment, where carbonate biomineralisation was strongly suppressed. This distribution suggests that formation of the sunflower-like architecture is intrinsically linked to the carbonate crystallisation process rather than to the chemistry of the incorporated metals. The persistence of this morphology despite the markedly different crystallogenetic pathways followed by Pb, Co and Cr indicates that aggregate architecture and metal partitioning evolved largely independently under the conditions investigated.

This morphological conservation is compatible with crystallisation pathways involving transient precursor phases rather than exclusively classical ion-by-ion crystal growth. Calcium carbonate is increasingly recognised as a model system in which crystallisation may proceed through prenucleation clusters, amorphous calcium carbonate (ACC) and other transient precursor phases before the formation of stable crystalline products (Gebauer et al., 2008; De Yoreo et al., 2015; Smeets et al., 2015). In biomineral and biomimetic systems, organic macromolecules may further influence these processes by interacting with dissolved ions, precursor phases and crystal growth surfaces, thereby modifying nucleation kinetics, crystal orientation and aggregate morphology (Gower & Odom, 2000; Aizenberg et al., 2002; Gower, 2008). Similar effects have been demonstrated in biological carbonate systems, where organic matrices and shell-derived proteins strongly influence crystal habit and organisation (Feng et al., 2000). Collectively, these studies provide a plausible mechanistic framework for interpreting the radial carbonate architectures observed in the present study.

On this basis, we propose the conceptual crystallogenetic model illustrated in Fig. 11. The precursor phases themselves were not directly observed in the present study; consequently, the proposed pathway is inferred from the morphology of the final aggregates rather than from a directly documented transformation sequence. Under the strongly supersaturated conditions generated by urease-driven urea hydrolysis, amorphous calcium carbonate (ACC) or nanoparticulate precursor phases may initially form within the biomolecule-rich solution (Fig. 11a). These precursor particles may subsequently aggregate and densify into spheroidal precursor bodies (Fig. 11b), followed by nucleation of calcite nanocrystals at their surfaces (Fig. 11c). Initial outward crystal growth may produce the first petal-like calcite crystals (Fig. 11d), while continued radial growth around the precursor-derived core may progressively generate the mature sunflower-like aggregates (Fig. 11e), culminating in the fully developed structures observed by SEM (Fig. 11f). The proposed precursor-derived core is consistent with the central structures described in the preceding morphological analysis, although the transformation linking precursor development, crystal growth and the subsequent detachment of the central core cannot be resolved from the present observations.

Because all treatments were prepared using the same crude soybean extract, the individual contribution of extract-derived biomolecules cannot be distinguished from

that of the rapid carbonate supersaturation generated during ureolysis. Both factors may have contributed to the development of the observed aggregate morphology, but their relative importance cannot be determined from the present experiments. Consequently, the conceptual model proposed here should be regarded as a possible interpretation of the observed morphology rather than as a directly demonstrated crystallisation sequence.

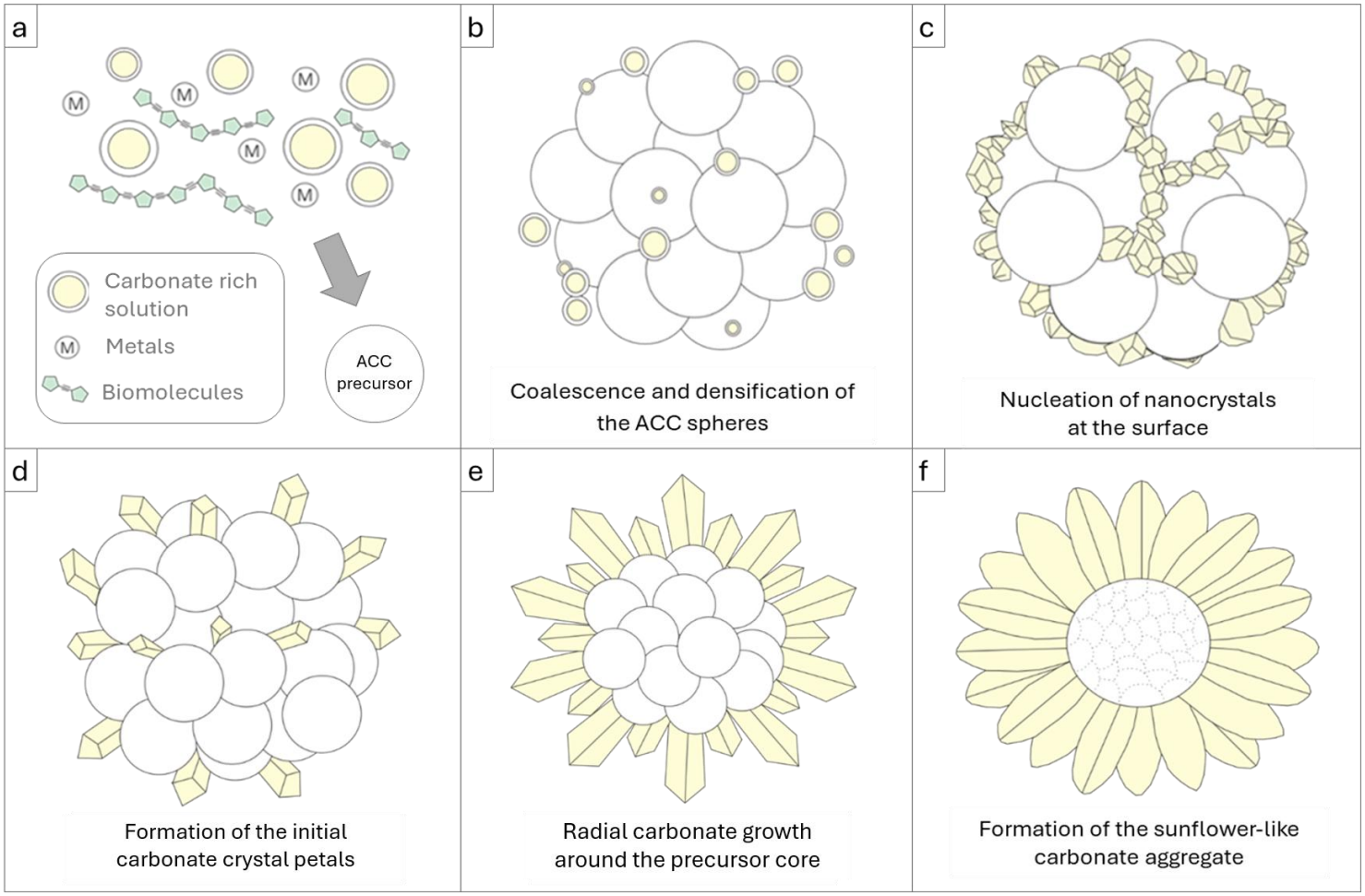

Figure 11. Proposed conceptual model illustrating a plausible crystallogenetic pathway for the formation of sunflower-like calcite aggregates during crude-enzyme-induced carbonate precipitation (EICP). (a) In a bicarbonate-rich mother solution generated by urease-driven urea hydrolysis, biomolecules interact with dissolved ions and metals, favouring the formation of amorphous calcium carbonate (ACC) or nanoparticulate precursor phases. (b) ACC spheres aggregate, coalesce and densify to form larger precursor bodies. (c) Nucleation of calcite nanocrystals initiates at the surface of these precursor domains. (d) Outward growth of the first calcite crystals produces initial petal-like units. (e) Continued radial calcite growth develops around a precursor-derived core. (f) Formation of the final sunflower-like calcite aggregate characterised by a precursor-derived core surrounded by radially organised calcite crystals.

5. Conclusions

Under an identical crude-enzyme EICP protocol, Pb, Co and Cr followed distinct crystallogenetic pathways governed primarily by their intrinsic geochemistry. Although all three metals were efficiently immobilised, their mineralogical fate diverged markedly, demonstrating that aqueous removal efficiency alone provides an incomplete description of contaminant immobilisation during carbonate biomineralisation.

Pb exhibited progressive mineralogical partitioning, evolving from predominantly Pb-bearing Ca-carbonate biominerals towards the stabilisation of discrete cerussite populations as metal loading increased. In contrast, Co remained diffusely associated with calcite-type carbonate biominerals across the entire concentration range, showing only modest compositional enrichment across all treatments, without the development of an independent crystalline Co-bearing phase. Chromium followed a fundamentally different trajectory: carbonate biomineralisation remained dominant at low and intermediate loadings but became progressively disrupted at the highest metal loading, where sulphate-associated precipitation emerged alongside marked reductions in both carbonate production and overall immobilisation efficiency. Together, these contrasting behaviours highlight the strong control exerted by metal geochemistry on the crystallogenetic pathways governing contaminant retention during EICP.

Sunflower-like carbonate aggregates developed across all systems in which carbonate biomineralisation remained active, irrespective of metal identity, indicating that metal-specific crystallogenetic pathways modified mineralogical fate without fundamentally altering the morphogenetic pathway responsible for the development of this characteristic carbonate crystal morphology. Their disappearance only under the strongest suppression of carbonate precipitation (Cr-T3) further supports the close association between this distinctive morphology and successful carbonate biomineralisation.

The distinct crystallogenetic pathways identified in this study indicate that the long-term stability of immobilised contaminants is likely to depend more strongly on the identity of their mineralogical hosts and the internal distribution of metals within those hosts than on carbonate precipitation alone. These implications are derived from single-metal systems and, in the absence of direct dissolution or long-term persistence experiments, remain inferred from phase identity and established mineral stability relationships. Nevertheless, the contrasting mineralogical products formed by Pb, Co and Cr indicate that contaminant-specific geochemistry governs not only immobilisation efficiency but also the nature of the resulting mineralogical hosts and their potential long-term behaviour.

Overall, the present findings show that effective metal immobilisation during crude-enzyme EICP arises from the interplay between aqueous metal geochemistry, biomineralisation processes and crystallogenetic pathway selection. This study establishes metal-specific crystallogenesis as a valuable framework for understanding contaminant partitioning during enzyme-induced carbonate precipitation and provides a geochemical basis for predicting how metal chemistry governs mineralisation pathway development and, ultimately, contaminant fate.

References

Addadi, L. and Weiner, S. (1992), Control and Design Principles in Biological Mineralization. Angew. Chem. Int. Ed. Engl., 31: 153-169. https://doi.org/10.1002/anie.199201531

Aizenberg, J., Lambert, G., Weiner, S., Addadi, L., 2002. Factors Involved in the Formation of Amorphous and Crystalline Calcium Carbonate: A Study of an Ascidian Skeleton. *Journal of the American Chemical Society* 124 (1), 32–39. https://doi.org/10.1021/ja016990l

Beniash, E., Aizenberg, J., Addadi, L., & Weiner, S. (1997). Amorphous calcium carbonate transforms into calcite during sea urchin larval spicule growth. *Proceedings of the Royal Society of London. Series B: Biological Sciences*, *264*(1380), 461–465. https://doi.org/10.1098/rspb.1997.0066

Bian, Y., Chen, Y., Zhan, L., Guo, H., Ke, H., Wang, Y., Wang, Q., Gao, Y., & Gao, Y. (2024). Effects of enzyme-induced carbonate precipitation technique on multiple heavy metals immobilization and unconfined compressive strength improvement of contaminated sand. *Science of the Total Environment*, *947*. https://doi.org/10.1016/j.scitotenv.2024.174409

Bourg, I. C., & Sposito, G. (2007). Molecular dynamics simulations of kinetic isotope fractionation during the diffusion of ionic species in liquid water. Geochimica et Cosmochimica Acta, 71(23), 5583–5589. https://doi.org/10.1016/j.gca.2007.01.021

Callagon, E., Fenter, P., Nagy, K. L., & Sturchio, N. C. (2014). Incorporation of Pb at the Calcite (104)–Water Interface. *Environmental Science & Technology*, 48(16), 9263–9269. https://doi.org/10.1021/es5014888

Callagon, E. B. R., Lee, S. S., Eng, P. J., Laanait, N., Sturchio, N. C., Nagy, K. L., & Fenter, P. (2017). Heteroepitaxial growth of cadmium carbonate at dolomite and calcite surfaces: Mechanisms and rates. *Geochimica et Cosmochimica Acta*, *205*, 360–380. https://doi.org/10.1016/j.gca.2016.12.007

de Yoreo, J. J., Gilbert, P. U. P. A., Sommerdijk, N. A. J. M., Penn, R. L., Whitelam, S., Joester, D., Zhang, H., Rimer, J. D., Navrotsky, A., Banfield, J. F., Wallace, A. F., Michel, F. M., Meldrum, F. C., Cölfen, H., & Dove, P. M. (2015). Crystallization by particle attachment in synthetic, biogenic, and geologic environments. *Science*, *349*(6247). https://doi.org/10.1126/science.aaa6760

Doebelin, N., & Kleeberg, R. (2015). *Profex* : a graphical user interface for the Rietveld refinement program *BGMN*. *Journal of Applied Crystallography*, *48*(5), 1573–1580. https://doi.org/10.1107/S1600576715014685

Fang, Z., Liu, W., Yao, T., Zhou, G., Wei, S., & Qin, L. (2022). Experimental study of chromium (III) coprecipitation with calcium carbonate. Geochimica et Cosmochimica Acta, 322, 94–108. https://doi.org/10.1016/j.gca.2022.01.019

Feng, Q.L., Pu, G., Pei, Y., Cui, F.Z., Li, H.D., Kim, T.N., 2000. Polymorph and morphology of calcium carbonate crystals induced by proteins extracted from mollusk shell. *Journal of Crystal Growth* 216 (1–4), 459–465. https://doi.org/10.1016/S0022-0248(00)00396-1

Freij, S. J., Putnis, A., & Astilleros, J. M. (2004). Nanoscale observations of the effect of cobalt on calcite growth and dissolution. *Journal of Crystal Growth*, *267*(1–2), 288–300. https://doi.org/10.1016/j.jcrysgro.2004.03.044

García-Sánchez, A., & Álvarez-Ayuso, E. (2002). Sorption of Zn, Cd and Cr on calcite. Application to purification of industrial wastewaters. *Minerals Engineering*, *15*(7), 539–547. https://doi.org/10.1016/S0892-6875(02)00072-9

Gebauer, D., Völkel, A., & Cölfen, H. (2008). Stable Prenucleation Calcium Carbonate Clusters. *Science*, *322*(5909), 1819–1822. https://doi.org/10.1126/science.1164271

González-López, J., Ruiz-Hernández, S.E., Fernández-González, Á., Jiménez, A., de Leeuw, N.H., Grau-Crespo, R., 2014. Cobalt incorporation in calcite: Thermochemistry of $(Ca,Co)CO_3$ solid solutions from density functional theory simulations. *Geochimica et Cosmochimica Acta* 142, 205–216. https://doi.org/10.1016/j.gca.2014.07.026

Gower, L. B. (2008). Biomimetic model systems for investigating the amorphous precursor pathway and its role in biomineralization. *Chemical Reviews*, *108*(11), 4551–4627. https://doi.org/10.1021/cr800443h

Gower, L. B., & Odom, D. J. (2000). Deposition of calcium carbonate films by a polymer-induced liquid-precursor (PILP) process. *Journal of Crystal Growth*, *210*(4), 719–734. https://doi.org/10.1016/S0022-0248(99)00749-6

Hamdan, N., & Kavazanjian, E. (2016). Enzyme-induced carbonate mineral precipitation for fugitive dust control. *Géotechnique*, *66*(7), 546–555. https://doi.org/10.1680/jgeot.15.P.168

Katsikopoulos, D., Fernández-González, Á., Prieto, A. C., & Prieto, M. (2008). Co-crystallization of Co(II) with calcite: Implications for the mobility of cobalt in aqueous

environments. *Chemical Geology*, *254*(1–2), 87–100. https://doi.org/10.1016/j.chemgeo.2008.06.003

Kidanemariam, T.G., Gebru, K.A. & Kidane Gebretinsae, H. A mini review of enzyme-induced calcite precipitation (EICP) technique for eco-friendly bio-cement production. *Environ Sci Pollut Res* 31, 16206–16215 (2024). https://doi.org/10.1007/s11356-023-31555-9

Kim, Y., Abdilla, B., Yuan, K., De Andrade, V., Sturchio, N. C., Lee, S. S., & Fenter, P. (2021). Replacement of Calcium Carbonate Polymorphs by Cerussite. *ACS Earth and Space Chemistry*, 5(9), 2433–2441. https://doi.org/10.1021/acsearthspacechem.1c00177

Kim, Y., Tekawade, A., Lee, S. S., & Fenter, P. (2023). Morphological and crystallographic controls in the replacement of calcite and aragonite by cerussite and otavite. *Geochimica et Cosmochimica Acta*, 341, 16–27. https://doi.org/10.1016/j.gca.2022.11.010

Langmuir, D. (1997) Aqueous Environmental Geochemistry. Prentice-Hall, Inc., Englewood Cliffs, 601.

Lorens, R. B. (1981). Sr, Cd, Mn and Co distribution coefficients in calcite as a function of calcite precipitation rate. Geochimica et Cosmochimica Acta, 45(4), 553–561. https://doi.org/10.1016/0016-7037(81)90188-5

Lowenstam, H. A., & Weiner, S. (1989). *On Biomineralization*. Oxford University Press. https://doi.org/10.1093/oso/9780195049770.001.0001

McBride, M.B. (1980), Chemisorption of Cd2+ on Calcite Surfaces. Soil Science Society of America Journal, 44: 26-28. https://doi.org/10.2136/sssaj1980.03615995004400010006x

Moghal, A. A. B., Lateef, M. A., Abu Sayeed Mohammed, S., Ahmad, M., Usman, A. R. A., & Almajed, A. (2020). Heavy Metal Immobilization Studies and Enhancement in Geotechnical Properties of Cohesive Soils by EICP Technique. *Applied Sciences*, *10*(21), 7568. https://doi.org/10.3390/app10217568

Nemati, M. & Voordouw, G. (2003). Modification of porous media permeability, using calcium carbonate produced enzymatically in situ. *Enzyme and Microbial Technology*, *33*(5), 635–642. https://doi.org/10.1016/S0141-0229(03)00191-1

Paquette, J., & Reeder, R. J. (1990). New type of compositional zoning in calcite: Insights into crystal-growth mechanisms. *Geology, 18*(12), 1244–1247. https://doi.org/10.1130/0091-7613(1990)018%3C1244:NTOCZI%3E2.3.CO;2

Paquette, J., Ward, W.B., Reeder, R.J. (1993). Compositional Zoning and Crystal Growth Mechanisms in Carbonates: A New Look at Microfabrics Imaged by Cathodoluminescence Microscopy. In: Rezak, R., Lavoie, D.L. (eds) Carbonate Microfabrics. Frontiers in Sedimentary Geology. Springer, New York, NY. https://doi.org/10.1007/978-1-4684-9421-1_18

Paquette, J., & Reeder, R. J. (1995). Relationship between surface structure, growth mechanism, and trace element incorporation in calcite. *Geochimica et Cosmochimica Acta, 59*(4), 735–749. https://doi.org/10.1016/0016-7037(95)00004-J

Rai, D., Moore, D.A., Hess, N.J. *et al.* Chromium(III) Hydroxide Solubility in the Aqueous K^+-H^+-OH^--CO_2-HCO^-_3-CO^{2-}_3-H_2O System: A Thermodynamic Model. *J Solution Chem* 36, 1261–1285 (2007). https://doi.org/10.1007/s10953-007-9179-5

Reeder, R. J. (1996). Interaction of divalent cobalt, zinc, cadmium, and barium with the calcite surface during layer growth. In *Pergamon Geochimica et Cosmochimica Acta* (Vol. 60, Issue 9). https://doi.org/10.1016/0016-7037(96)00034-8

Riechers, S. L., Ilton, E. S., Qafoku, O., Du, Y., & Kerisit, S. N. (2022). Cobalt hydroxide–cobalt carbonate competitive growth on carbonate surfaces. *Chemical Geology*, *605*. https://doi.org/10.1016/j.chemgeo.2022.120951

Smeets, P. J. M., Cho, K. R., Kempen, R. G. E., Sommerdijk, N. A. J. M., & de Yoreo, J. J. (2015). Calcium carbonate nucleation driven by ion binding in a biomimetic matrix revealed by in situ electron microscopy. *Nature Materials*, *14*(4), 394–399. https://doi.org/10.1038/nmat4193

Solé, V.A., Papillon, E., Cotte, M., Walter, P., Susini, J., 2007. A multiplatform code for the analysis of energy-dispersive X-ray fluorescence spectra. *Spectrochimica Acta Part B: Atomic Spectroscopy* 62 (1), 63–68. https://doi.org/10.1016/j.sab.2006.12.002

Stipp, S.L., Hochella, M.F., Parks, G.A., Leckie, J.O., 1992. Cd^{2+} uptake by calcite, solid-state diffusion, and the formation of solid solution: Interface processes observed with near-surface sensitive techniques (XPS, LEED, and AES). *Geochimica et Cosmochimica Acta* 56 (5), 1941–1954. https://doi.org/10.1016/0016-7037(92)90321-9.

Stumm, W. and Morgan, J.J. (1996) Aquatic Chemistry, Chemical Equilibria and Rates in Natural Waters. 3rd Edition, John Wiley & Sons, Inc., New York.

Sturchio, N. C., Chiarello, R. P., Cheng, L., Lyman, P. F., Bedzyk, M. J., Qian, Y., You, H., Yee, D., Geissbuhler, P., Sorensen, L. B., Liang, Y., & Baer, D. R. (1997). Lead adsorption at the calcite-water interface: Synchrotron X-ray standing wave and X-ray reflectivity studies. *Geochimica et Cosmochimica Acta*, *61*(2), 251–263. https://doi.org/10.1016/S0016-7037(96)00326-2

Tolentino, H.C.N., Geraldes, R.R., Silva, Moreno, G. B. Z. L. "TARUMÃ station for the CARNAÚBA beamline at SIRIUS/LNLS", Proc. SPIE 11112, X-Ray Nanoimaging: Instruments and Methods IV, 1111206 (9 Sept 2019); https://doi.org/10.1117/12.2531110

Tolentino, H.C.N., Geraldes, R.R., Silva, F.M.C., Guaita, M.G.D., Camarda, C.M., Szostak, R., Neckel, I.T., Teixeira, V.C., Hesterberg, D., Pérez, C.A., Galante, D., Callefo, F., Neto, A.C.P., Kofukuda, L.M., Sotero, A.P.S., Moreno, G.B.Z.L., Luiz, S.A.L., Bueno, C.S.N.C., Lena, F.R., Westfahl, H., 2023. The CARNAÚBA X-ray nanospectroscopy beamline at the Sirius-LNLS synchrotron light source: Developments, commissioning, and first science at the TARUMÃ station. *Journal of Electron Spectroscopy and Related Phenomena* 266, 147340. https://doi.org/10.1016/j.elspec.2023.147340

Weiner, S., & Dove, P. M. (2003). An Overview of Biomineralization Processes and the Problem of the Vital Effect. *Reviews in Mineralogy & Geochemistry*, *54*(1), 1–29. https://doi.org/10.2113/0540001

Weiner, S., & Addadi, L. (2011). Crystallization Pathways in Biomineralization. *Annual Review of Materials Research*, *41*(1), 21–40. https://doi.org/10.1146/annurev-matsci-062910-095803

Whiffin, V. (2004) Microbial CaCO3 Precipitation for the Production of Biocement. PhD Thesis, Murdoch University, Perth. Microbial CaCO3 precipitation for the production of biocement - Murdoch University

Whiffin, V. S., van Paassen, L. A., & Harkes, M. P. (2007). Microbial Carbonate Precipitation as a Soil Improvement Technique. *Geomicrobiology Journal*, *24*(5), 417–423. https://doi.org/10.1080/01490450701436505

Xu, M., Ilton, E. S., Engelhard, M. H., Qafoku, O., Felmy, A. R., Rosso, K. M., & Kerisit, S. (2015). Heterogeneous growth of cadmium and cobalt carbonate phases at the (10$\bar{1}$4) calcite surface. Chemical Geology, 397, 24–36. https://doi.org/10.1016/j.chemgeo.2015.01.003

Yasuhara, H., Neupane, D., Hayashi, K., & Okamura, M. (2012). Experiments and predictions of physical properties of sand cemented by enzymatically-induced

carbonate precipitation. *Soils and Foundations, 52*(3), 539–549. https://doi.org/10.1016/j.sandf.2012.05.011

Yuan, K., De Andrade, V., Feng, Z., Sturchio, N.C., Lee, S.S., Fenter, P., (2018). Pb^{2+}–calcite interactions under far-from-equilibrium conditions: Formation of micropyramids and pseudomorphic growth of cerussite. *The Journal of Physical Chemistry C* 122, 2238–2247. https://doi.org/10.1021/acs.jpcc.7b11682

Yuan, K., Lee, S. S., De Andrade, V., Sturchio, N. C., & Fenter, P. (2016). Replacement of calcite by cerussite. Environmental Science & Technology, 50(23), 12984–12991. https://doi.org/10.1021/acs.est.6b03911

Zeng, H., Jin, B., Xu, S., Han, L., Wang, J., Jia, H., Dapaah, M. F., & Cheng, L. (2025). Removal of copper, lead and cadmium from water through enzyme-induced carbonate precipitation by soybean urease. *Environmental Research*, *277*. https://doi.org/10.1016/j.envres.2025.121610

CRediT authorship contribution statement

Heloísa Dickinson: Conceptualization, Methodology, Investigation, Formal analysis, Data curation, Visualization, Writing – original draft, Writing – review & editing.
John MacDonald: Supervision, Visualization, Methodology, Writing – review & editing.
Carlos Alberto Pérez: Resources, Writing – review & editing.
Jaime L. Toney: Supervision, Writing – review & editing, Funding acquisition.

Acknowledgements:

The authors gratefully acknowledge Liene Spruzeniece, Manager of the Electron Microscopy Facility (GEMS), University of Glasgow, for her technical support with electron microscopy analyses. We also thank Connor Brolly, Technician in the School of Geographical and Earth Sciences, University of Glasgow, for his invaluable technical assistance throughout the experimental work. We are grateful to Gavin Sim, Analytical Services Manager, School of GeoSciences, University of Edinburgh, for his assistance with the ammonium analytical measurements.